# Heterogeneous nickel isotope compositions of the terrestrial mantle - Part 2: Mafic lithologies

**Naomi J. Saunders*[1,2]; Jane Barling[1]; Jason Harvey[3]; J. Godfrey Fitton[4]; Alex N. Halliday[1,2]**

[1]Dept of Earth Sciences, University of Oxford, South Parks Road, Oxford, OX1 3AN, UK

[2]Lamont-Doherty Earth Observatory, Columbia University, 61 Route 9W, Palisades, USA, 10964

[3]School of Earth and Environment, University of Leeds, Leeds, LS2 9JT, UK

[4]School of GeoSciences, University of Edinburgh, The King's Buildings, James Hutton Road, Edinburgh, EH9 3FE, UK

*naomi.saunders@mail.com, ORCID https://orcid.org/0000-0002-3622-946X

## Highlights

- Significant $\delta^{60/58}$Ni heterogeneities found in mafic rocks
- Mean $\delta^{60/58}$Ni is the same for MORB and OIB
- No evidence of fractionation in $\delta^{60/58}$Ni with partial melting or crystal fractionation
- Geochemical signatures of enrichment correlate with light $\delta^{60/58}$Ni
- Mixing in the mantle with enriched recycled material may be responsible

## Abstract

We report stable Ni isotope compositions ($\delta^{60/58}$Ni, relative to SRM986) for mafic lavas with a range of -0.16 ‰ to +0.20 ‰ (n=44), similar to that of peridotite samples. Ocean island basalts (OIB) have been analysed from Iceland (n=6), the Azores (n=3), the Galápagos Islands (n=2), and Lō‘ihi, Hawaii (n=1). Samples from Iceland (average $\delta^{60/58}$Ni = +0.13±0.16‰, 2s, n=7) display the greatest range in Ni isotope compositions from a single OIB location in this work, of +0.01 ‰ to +0.23 ‰. Samples from the Azores (average $\delta^{60/58}$Ni = -0.10±0.10 ‰, 2s) and Galápagos (average $\delta^{60/58}$Ni = -0.01±0.04 ‰, 2s) are generally isotopically lighter. The single Lō‘ihi sample has a $\delta^{60/58}$Ni of +0.17 ‰. The lightest analysed bulk rock $\delta^{60/58}$Ni in this work, -0.16 ‰, is from the Azores island, Pico. Enriched mid ocean ridge basalts (E-MORB), which have $(La/Sm)_N>1$, are isotopically lighter than normal type MORB (N-MORB), as shown by data from the Mid Atlantic Ridge (n=9) and East Pacific Rise (n=3). All E-MORB average $\delta^{60/58}$Ni =

+0.00±0.06 ‰ (2s, n=7), whereas N-MORB average $\delta^{60/58}$Ni = +0.14±0.10 ‰ (2s, n=5).

A suite of 15 mafic samples from the Cameroon Line, comprising lithologies ranging from nephelinites to hypersthene-normative basalts, have Ni isotope compositions that are identical within analytical uncertainty (average $\delta^{60/58}$Ni = +0.08±0.06 ‰, 2s). Similarly, MORB samples display no relationship between $\delta^{60/58}$Ni and geochemical indicators of degree of partial melting or fractional crystallisation. Host lavas for two previously analysed ultramafic xenolith suites have $\delta^{60/58}$Ni identical to the average $\delta^{60/58}$Ni of their respective xenolith suites. This is consistent with previously published evidence from peridotites and komatiites that Ni isotopes are not greatly fractionated by melting. Therefore, mafic rocks may preserve the $\delta^{60/58}$Ni of their mantle source. Sampling a greater volume of mantle, their average Ni isotope composition +0.07±0.17 ‰ (2s, n=44) may also be a better representation of the Bulk Silicate Earth (BSE), than estimates based purely on peridotites.

The $\delta^{60/58}$Ni of MORB co-varies with La/Sm, Rb/Sr, europium anomaly (Eu/Eu*), and $K_2O/(K_2O+Na_2O)$. The relationships between these parameters and $\delta^{60/58}$Ni are consistent with mixing between two model endmembers. One could be depleted MORB or depleted MORB mantle (DMM) with a relatively heavy Ni isotope composition; the other a more enriched endmember that has isotopically lighter $\delta^{60/58}$Ni. The link between lighter $\delta^{60/58}$Ni and enriched lithologies in the mantle is further supported by published evidence of light Ni isotope compositions associated with some pyroxenite xenoliths. However, the curvature of the apparent mixing arrays defined by basalts is hard to reconcile with admixing of geochemically enriched but isotopically fractionated oceanic crustal lithologies. High [Ni] enriched magmas such as kimberlites may be a closer match to the enriched endmember. However, this needs further study.

## Keywords

**Stable isotopes, Nickel, OIB, MORB, Mantle recycling**

## 1. Introduction

Nickel (Ni) is an iron-peak, first-row transition metal with five stable isotopes: $^{58}$Ni (68.08 %), $^{60}$Ni (26.22 %), $^{61}$Ni (1.11 %), $^{62}$Ni (3.64 %), and $^{64}$Ni (0.93 %) (Gramlich et al., 1989). Nickel is always divalent

54 under mantle oxidation conditions (Nicholls, 1974), and substitutes readily for magnesium in mantle
55 silicates. Therefore, Ni is highly concentrated in olivine, and to a lesser degree in other ferromagnesian
56 silicates, and is highly compatible during mantle melting, due to the similar ionic radii of Ni and Mg (83 pm
57 relative to 86 pm; Shannon, 1976). As a result, only approximately 0.03 % of the silicate Earth's Ni budget
58 has accumulated in the continental crust over geological time (McDonough and Sun, 1995).

59 Investigation of the isotope composition of Ni in mantle-derived materials provides the opportunity to
60 elucidate mantle processes without the complicating effects associated with changes in oxidation state, such
61 as is observed in Fe isotopic studies (e.g. Williams et al., 2004; Sossi et al., 2012). Iron also substitutes for
62 Mg in mantle silicates in a similar way to Ni. Stable Ni isotope compositions are reported in standard delta
63 notation as the difference between the ratio of $^{60}$Ni to $^{58}$Ni in a sample relative to the same in SRM986
64 ($\delta^{60/58}$Ni, ‰). Published Ni isotope composition for mafic and ultramafic samples are presented in Figure 1.
65 Early $\delta^{60/58}$Ni data for products of mantle melting were limited, however, more recent work has greatly
66 expanded available data (see references in Figure 1).

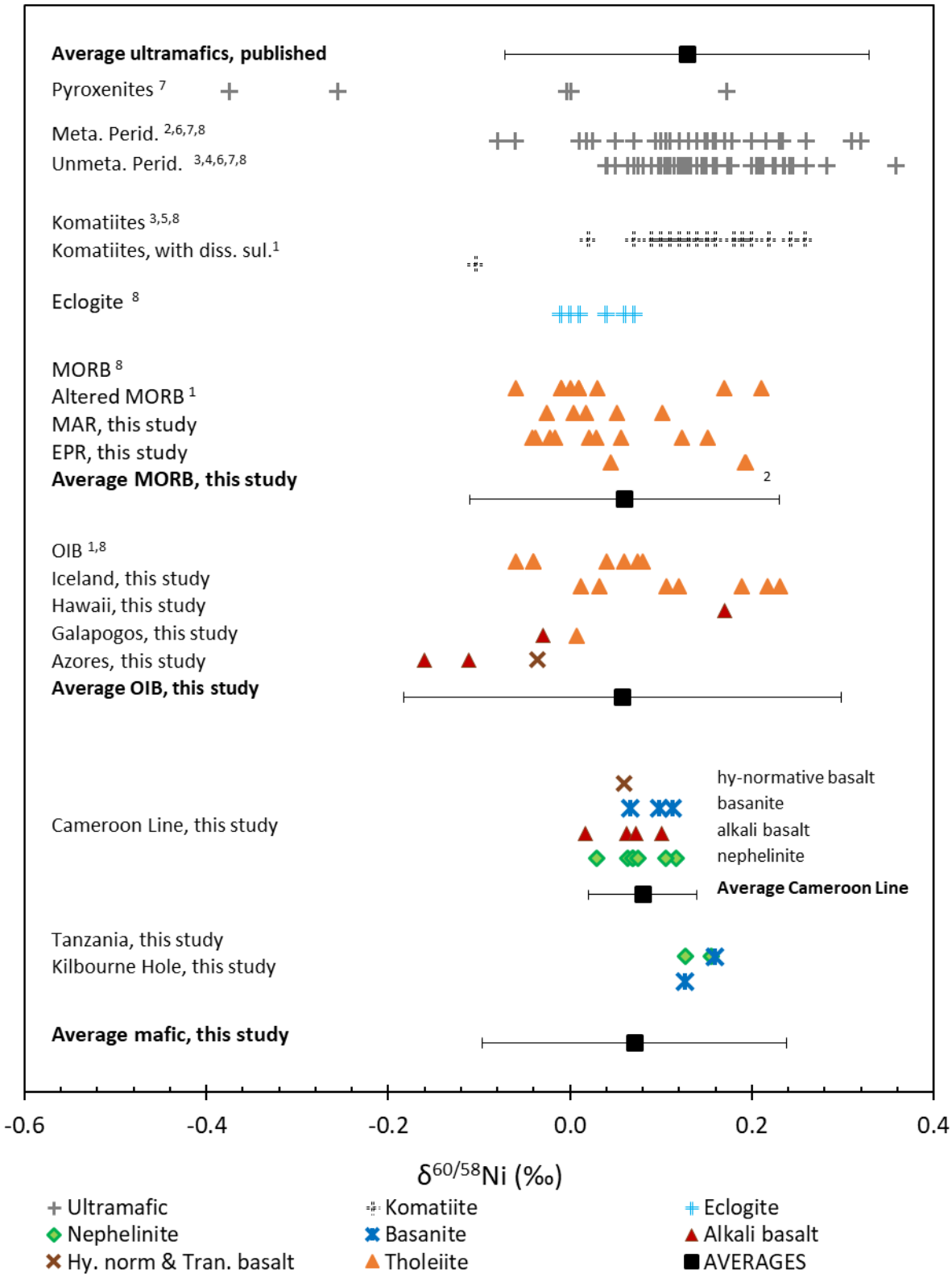


**Figure 1**

Nickel isotope compositions of samples of MORB, OIB, and other intraplate volcanism, separated by geographical locality and lithology, and published data for ultramafic, komatiite, and eclogite samples.

(1) Gueguen et al., 2013; (2) Ratié et al., 2015; (3) Gall et al., 2017; (4) Spivak-Birndorf et al., 2018; (5) Wang et al., 2019; (6) Klaver et al., 2020; (7) Saunders et al., 2020; (8) Wang et al., 2021

The average peridotite $\delta^{60/58}$Ni = +0.13±0.20 ‰ (2s, n=99; all published peridotite samples). The average $\delta^{60/58}$Ni of all mafic bulk-rock samples from this work (+0.07±0.17 ‰, 2s, n=44).

Ultramafic includes only peridotites and pyroxenites, from both massif and xenolith. Hy. norm = hypersthene-normative basalt. Tran. basalt = transitional basalt. The Cameroon Line includes several volcanic centres in the Gulf of Guinea (Bioko and Principe) and Cameroon (Bambouto, Mt Cameroon, Mandara Mountains, Manengouba, and Etinde). No variation in Ni isotope composition is found between Cameroon Line locations or between different lithologies. Intermediate precision (2s) of this work in Ni isotope composition is ±0.06 ‰.

Published Ni isotope compositions for mid ocean ridge basalts (MORB) vary from -0.22 ‰ to +0.24 ‰ (Cameron et al., 2009; Gall, 2011; Gueguen et al., 2013; Wang et al., 2021). The extremes of this range however, are limited to the earliest published works, with the most recent data having a smaller $\delta^{60/58}$Ni range (-0.06 ‰ to +0.21 ‰; Wang et al., 2021). Early work by Gall (2011) suggested that MORB were, on average, lighter than the available published estimate for BSE from Steele et al. (2011). It was hence suggested that Ni isotopes fractionate with partial melting, with lighter isotopes preferentially enriched in the melt phase during melting (Gall, 2011), as suggested for Fe isotopes (Williams et al., 2004; Williams et al., 2005; Weyer et al., 2007; Williams et al., 2009; Teng et al., 2013). However, no relationship was found between $\delta^{60/58}$Ni of peridotites and degree of melt depletion (Klaver et al., 2020). Similarly, komatiites (>45 % partial melting) have identical average Ni isotope compositions to peridotites (Wang et al., 2021). A hint of a difference between mafic samples and peridotites is reported in Wang et al. (2021), although the two populations overlap considerably (mafic $\delta^{60/58}$Ni average +0.03±0.16 ‰, 2s (where 2s denotes 2 standard deviations), n=15; peridotite $\delta^{60/58}$Ni average +0.10±0.07 ‰, 2s, n=13). Eclogites formed from basalts in subduction zones have a comparable average $\delta^{60/58}$Ni value to basalts of +0.02±0.06 ‰ (2s, n=7; Wang et al., 2021).

Nickel isotope differences between coexisting mantle minerals are limited (Saunders et al., 2020), apparently endorsing the case for minimal fractionation during melting. However, this does not in itself establish that melting does not lead to fractionation because liquids could be consistently lighter than peridotite minerals. Furthermore, Saunders et al. (2020) showed that the isotopic fractionation between clinopyroxene and orthopyroxene is dependent on mineral and bulk rock chemical composition. Indeed, this clinopyroxene – orthopyroxene difference, though small, correlates with bulk rock indices of geochemical enrichment. Clinopyroxene is progressively lighter relative to orthopyroxene in rocks with high U, La/Yb, and Fe/Mg and more negative (lighter) bulk $\delta^{60/58}$Ni (Saunders et al., 2020). Therefore, small isotopic fractionations are

being produced at the mineral scale in a manner that relates to peridotite composition and enriched signatures.

So far, the database for basaltic samples to compare this with is not extensive. To date, only 7 samples from Hawaii (Gueguen et al., 2013; Wang et al., 2021) and geological reference materials (e.g. BHVO2, BIR1) comprise the published $\delta^{60/58}$Ni data for ocean island basalts (OIB). Consequently, the present work represents a more detailed study of mafic lavas in order to better understand the apparently conflicting conclusions from prior studies of basalts and peridotites. This work also looks at E-MORB and N-MORB, and is the first to study more than one ocean island as an indication of deep mantle heterogeneity.

## 2. Geological setting and sample descriptions

Twelve mid ocean ridge basalts (MORB) from the Atlantic and Pacific Oceans, and twelve ocean island basalt (OIB) samples were analysed in this work. In addition, a suite of seventeen samples from other intraplate volcanic settings were analysed including; from the Cameroon Line and the East African Rift (Tanzania). All samples have been selected to be as unaffected as possible by post-eruption subaerial alteration. Previously published major and trace element characterisation of these samples (where available) can be found, with references, in Table EA1 and EA2. Mafic samples with available radiogenic isotopic data (Halliday et al., 1990; Halliday et al., 1992; Dosso et al., 1999; Harpp and White, 2001) have a relatively small unenriched compositional range (e.g. $\varepsilon^{143}$Nd = 2.3 to 10.0, Table EA3).

### 2.1 Mid ocean ridges

The MORB samples were selected for this study from optically unaltered glass chips from between 36 ° and 37 °N on the Mid Atlantic Ridge (MAR) (n=9) and from between 5 ° and 15 °N on the East Pacific Rise (EPR) (n=3). The MAR samples were dredged using a manned submersible during the 1992 FAZAR expedition (French American Atlantic Ridge cruise), from depths >1000 meters below sea level (Yi et al., 2000). The EPR samples are a subset of samples from Niu and Batiza (1997), dredged from seamounts. Samples from both locations include both N- and E-MORB.

The Mid Atlantic Ridge is a slow spreading ridge, with rates of 25 mm·yr$^{-1}$ (Murton and Rona, 2015). The MAR samples come from a ridge region that shows a geochemical anomaly associated with the proximity of the Azores hotspot (Dosso et al., 1999). The region is characterized by large excesses in $^{230}Th/^{238}U$ and latitudinal variations in radiogenic isotopic ratios (e.g. Sr) and trace element data (Dosso et al., 1999).

The East Pacific Rise is a fast spreading ridge, with rates of 84 – 140 mm·yr$^{-1}$ (Niu and Batiza, 1997). The geochemistry of the EPR sample suite is consistent with derivation from two components in the mantle, one enriched and the other depleted in incompatible elements (Niu and Batiza, 1997). These are inferred to be physically small mantle domains, consistent with the observed heterogeneity in the chemical composition of lavas from single seamounts (Niu and Batiza, 1997).

### 2.2 Ocean islands

Samples from four ocean island groups were analysed in this study: Iceland, the Azores, Galápagos, and Hawaii. No samples had $K_2O/P_2O_5$ <1, the criterion used by Hauri (1996) to indicate post-eruption subaerial alteration, suggesting that all these samples are geochemically unaltered.

Iceland formed in the North Atlantic at the intersection of the Mid Atlantic Ridge (MAR) and a mantle plume with a relatively depleted composition (Kempton et al., 2000). The Iceland samples are all tholeiitic basalts, and were collected from the central west, north and east extremes of the island from subaerially erupted lava flows. The SNB series samples were collected from Snaefellsnes, an off-axis neo-volcanic zone, in central west Iceland (Kempton et al., 2000). The CX series (also known by prefix C; Watkins and Walker, 1977) are from Hjaleigulaekur, near Neskaupstaður, in eastern Iceland. GS18 (also known in some literature as GR18; Kristjansson et al., 2004) was collected from Granastaðir, and ST38 from Skaldsstaðir both close to 65°22′30″N, 018°15′29″W in the north of the island. Snaefellsnes lavas are of Quaternary age, unlike the samples from the other sites sampled which are of Neogene age (Hardarson and Fitton, 1997).

The Azores also formed from interaction of a mantle plume with the MAR, and consists of nine islands, which form three unequal groups based on the geographic relationship with each other and the ridge. Azores lavas exhibit extreme heterogeneity in isotopic and incompatible element compositions, even within single islands (White et al., 1979; Moreira et al., 1999; Beier et al., 2012), and can be relatively depleted in radiogenic isotopic composition (e.g. Nd, Os) and Fe-poor (Schaefer et al., 2002). The three samples

156 analysed here each come from a different island: Pico and Fayal (also spelled Faial) from the central group;
157 and Flores, from the western group. The former are alkali basalts, whereas the Flores sample is a transitional
158 basalt. All of the lavas are <10 Ma in age, and are petrographically relatively unaltered (Halliday et al.,
159 1995).

160 The Galápagos Islands lie just south of the fast-spreading ridge between the Nazca and Cocos plates.
161 Geochemical studies of Galápagos basalts suggest that they formed from a mantle plume containing a
162 depleted N-MORB-like component (White et al., 1993). Harpp and White (2001) proposed four isotopically
163 distinct end-members, three geographically restricted plume components and DMM. Both Galápagos
164 samples analysed in this work (one tholeiite, one alkali basalt) were dredged from the north-west of the
165 island cluster (Harpp and White, 2001) and originate from 2200 metres below sea level (Yi et al., 2000).

166 The Emperor-Hawaii Island chain in the central-north Pacific is ~6000 km long, recording >81 Myr of the
167 Hawaiian mantle plume. Lō‘ihi is a seamount at the most recent and south-easternmost extreme of this chain.
168 The sample is an alkali basalt glass, dredged from 2500 metres below sea level (Yi et al., 2000). The sample
169 has olivine as a phenocryst phase and sulphide globules have been observed in both the basalt and the
170 phenocrysts (Yi et al., 2000).

171 **2.3 Other intraplate settings**

172 The other intraplate samples come from both the oceanic and continental sectors the Cameroon Line (n= 15),
173 two nephelinites from the East African Rift (Tanzania), and two host lavas from xenolith localities analysed
174 in Saunders et al. (2020): Lashaine, Tanzania; and Kilbourne Hole, USA. The samples selected range from
175 hypersthene-normative basalt, through alkali basalt and basanite (including ankaramite), to nephelinite; a
176 sequence of mafic compositions reflecting decreasing degrees of partial melting (e.g. Green, 1970).

177 The Cameroon Line is a highly unusual y-shaped intraplate alkaline volcanic province that transects the
178 ocean-continent boundary (Fitton, 1987). It extends ~1600 km from the Ngaoundéré plateau (Cameroon) in
179 the northeast, through many volcanic centres in Cameroon, to the volcanic islands of Bioko, São Tomé,
180 Príncipe, and Annobón (also known as Pagalu), in the Atlantic Ocean to the southwest. The origins of the
181 Cameroon Line have been disputed (e.g. Fitton and Dunlop, 1985; Lee et al., 1994; Atouba et al., 2016;

Guimarães et al., 2020). The only currently active volcano is Mount Cameroon, which last erupted in 2000 (Suh et al., 2008).

The volcanic centres sampled for this study are (from NE to SW): Mandara Mountains, Bambouto, Manengouba, Mt Cameroon and nearby Etinde, and two islands (Bioko, Principe). Although two samples (C134, C146) from this section had $K_2O/P_2O_5$ <1 (a criterion suggested by Hauri (1996) to indicate post-eruption subaerial alteration) most of the Cameroon Line samples are unaffected by surface alteration.

Two further intraplate nephelinites were analysed from Tanzania to complement the nephelinite samples from the Cameroon Line. Kwaraha is a nephelinitic pyroclastic cone on the East African Rift. A single carbonatite flow is observed at this site (Dawson, 2012). The Kwaraha nephelinite has clinopyroxene and olivine as phenocryst phases and preserves Pb isotope disequilibrium between the bulk rock and the clinopyroxene that it contains (Paslick, 1995). Loolmurwak crater lies on the Monduli plains, on the East African Rift. The crater is dominated by nephelinite flows (Dawson and Smith, 1988). The sample from Loolmurwak was included as a lithological comparison from another volcanic system despite a lack of published data.

The host lavas for previously analysed xenoliths were from Lashaine, Tanzania; and Kilbourne Hole, USA. Lashaine (3°22'S, 36°26'E) is a tuff cone ~140 km NE of Kwaraha and ~90 km SE of Loolmurwak, on the Monduli plains on the eastern branch of the East African Rift. Kilbourne Hole (31°59'N, 106°57'W) is a volcanic maar to the east of the Late Pleistocene Potrillo Volcanic Field, located near the axis of the Rio Grande Rift. Both samples are basanites.

## 3 Analytical methods

Apart from the MORB and Lō'ihi samples, which were glass chips, samples analysed in this study were from pre-existing powders. The glass chips were optically examined to be free from surface alteration. In order to check that the pre-existing powders had not been contaminated with Ni (e.g. during crushing), Etinde nephelinite samples were also analysed; prepared by hand-crushing fresh chips in agate. These nephelinites have the lowest Ni concentration of all the studied samples and would have been the most

208 vulnerable to possible Ni contamination during their preparation. No evidence of contamination was detected
209 (see Electronic Appendix EA5 for the comparison of the data from these processing methods).

210 Analytical work was carried out in the Department of Earth Sciences, University of Oxford. All mineral
211 acids used in sample dissolution, column chemistry, and analysis were sub-boiling distilled in house and
212 diluted with ultrapure 18.2 MΩ·cm water. Samples were weighed into Savillex® PFA vials (~0.010 g to
213 0.55 g depending on Ni content) on a 5-figure balance, and double spike (25:75 mixture of $^{61}$Ni and $^{62}$Ni)
214 was accurately weighed to give 2.5 parts double spike Ni to 1 part natural Ni (Gall et al., 2012). A total of
215 3850 ng Ni was processed for each sample, of which 1100 ng was from the sample. Samples were digested
216 in two stages; the first using 2 ml of pre-mixed $HNO_3$:HF acid (3:1) on a hotplate. After the acids had
217 evaporated, sufficient 6M HCl (up to 5 ml) was added to bring the sample back into solution.

218 Nickel purification was carried out in a metal-free laboratory using the three-stage ion exchange chemistry of
219 Gall et al. (2012), using PTFE heat shrink micro-columns of diminishing size (column size; 615 µl, 250 µl,
220 and 120 µl).

221 In column 1, the first of two cation resin (AG50W-X4) columns, the load solution was a dilute mixture of
222 HCl, di-ammonium-hydrogen-citrate (dAHC), and ammonia. On this column, Ni, Zn, and Cu (the more
223 electronegative divalent cations) bind with ammonia while other elements, as citrate complexes, pass
224 through the column. Following the load solution, a short rinse of the dAHC and ammonia mixture ensured
225 all citrate complexes had eluted. A rinse of 0.4M HCl ensured all excess ammonia was removed from the
226 resin to waste. The Ni, Cu, and Zn, were then eluted in a 3M HCl solution. In column 2, the load solution
227 was dilute HCl and oxalic acid. Following the load solution, short rinses of the HCl and oxalic mixture
228 ensured that all matrix material had interacted with the resin, and $>2^+$ elements had eluted. Remaining
229 divalent elements were rinsed from the column as chloro-complexes with a second set of short rinses of HCl
230 and acetone, which also conditioned the resin for the final elution of Ni. The Ni was then selectively eluted
231 in a solution of dilute HCl and dimethylglyoxime (DMG) in acetone. Addition of ultrapure water in the
232 collection beaker and a low drying temperature (85 °C) were needed to prevent volatilisation of Ni in
233 acetone. In column 3, the only anion resin (AG1-X8) column, the load solution was 6M HCl and dilute
234 $H_2O_2$. Nickel was eluted immediately, whereas Fe formed chloro-complexes that remained on the resin in

6M HCl (Gall et al., 2012). Following the load solution, a short rinse of an HCl and $H_2O_2$ mixture ensured that all Ni had been eluted. After each column, the eluent was evaporated and refluxed in concentrated $HNO_3$ overnight in order to destroy organic molecules eluted with the Ni.

Some modifications were made to the published method of Gall et al. (2012), including an increase to the volume of the first-load solution to increase the amount of Ca and Mg that could be removed by the first column. A second 90 µl concentrated $HNO_3$ was added and dried down after the overnight reflux and dry-down of the Ni eluted from the final column. This final dry down was to ensure the destruction of column-related organics before dilution for analysis. For samples where >0.03 g sample was required to get 1100 ng nickel, a larger load volume was required to keep the sample in solution before the first column, and provide sufficient citrate for binding the matrix elements. The volume of the 5M HCl solution was increased until the sample was entirely in solution, and then further reagents added in proportion to make the correct load solution, with enough citrate to bind the Ca and Mg. This resulted in loads of up to 10 times the normal volume.

Nickel isotopes (58, 60, 61, and 62) were analysed in pseudo-high resolution on a Nu Plasma HR MC-ICPMS, with each collector using a $10^{11}$ Ω resistor, capable of measuring currents up to $10^{-10}$ A. The analysed masses were measured on the low mass peak shoulder in order to avoid variable polyatomic interferences, especially on mass 58. Mass 57 was monitored for correction of the isobaric interference of $^{58}$Fe on $^{58}$Ni. Each run included a peak centre, offset of the mass to the peak shoulder, followed by an ESA deflected baseline and then 30 ratios, of 15-second integration time. Two natural FeNi-sulphides were used as in-house standards to monitor the correction of the polyatomic and isobaric interferences. These were measured both unpurified (with Fe) and purified through column chemistry (no Fe). Sulphide Kambalda had an average $\delta^{60/58}$Ni of -0.89±0.08 ‰ (2s, where 2s throughout denotes 2 standard deviations, n=52) without chemistry purification, and -0.89±0.06 ‰ (2s, n=66) with chemistry. Sulphide Sudbury had an average $\delta^{60/58}$Ni of +0.76±0.06 ‰ (2s, n=53) without chemistry purification, and +0.77±0.05 ‰ (2s, n=60) with chemistry.

To further reduce the effect of any residual uncorrected polyatomic interferences or matrix effects, samples and standards were intensity matched at a total Ni signal of ~15 V. Data reduction for the deconvolution of

the double spike was done online using the procedures of Siebert et al. (2001) followed by offline normalisation to bracketing SRM986. Nickel concentrations were calculated by isotope dilution from the fractionation-corrected double spiked Ni ratios.

The accuracy and precision of our methods were assessed by repeated analysis of USGS reference materials in each analytical session. At least one USGS reference material (BHVO2, BIR1a, PCC1, or DTS2) was processed with each sample batch and analysed over more than one session. The resulting average Ni isotope compositions for BIR1 ($\delta^{60/58}$Ni = +0.15±0.06 ‰, 2s, n=20); BHVO2 ($\delta^{60/58}$Ni = +0.03±0.06 ‰, 2s, n=36); in addition to ultramafic USGS rock standards: PCC1 ($\delta^{60/58}$Ni = +0.14±0.06 ‰, 2s, n=17) and DTS2 ($\delta^{60/58}$Ni = +0.15±0.05 ‰, 2s, n=13); are all are within analytical uncertainty of the published values, except for the PCC1 value of Cameron et al. (2009), which is outside the range of all subsequent studies.

Based on the above analyses of rock reference materials the intermediate precision (within-laboratory reproducibility, equivalent to external reproducibility) of this study was assessed as ±0.06 ‰ (2s). This was equal to the maximum 2× standard deviation from the repeated replicates of USGS rock standards. This uncertainty is used for all representative error bars in the figures in this paper.

A total procedural Ni blank was analysed with each batch of column chemistry to monitor all potential Ni contamination from dissolution to dilution for analysis. These blanks were analysed on a Thermo-Finnigan™ Element 2, or PerkinElmer™ NexION Quad 350D ICPMS and showed an insignificant Ni blank of <3.7 ng, compared to an average sample and spike Ni load of ~4000 ng. Blanks for low-Ni samples that used large load solutions in the first column were higher by a factor of ~2, which remains insignificant in comparison to total Ni analysed.

## 4 Results

The Ni isotope compositions and concentrations for the samples in this work are presented in Table 1, and shown graphically in Figure 1, which also includes published data for comparison (see Figure 1 for references). The average $\delta^{60/58}$Ni for the mafic samples analysed in this study is +0.07±0.17 ‰ (2s, n=44). The mean of each major sample set (MORB, OIB, and samples from the Cameroon Line) are identical

288 within analytical uncertainty, and comparable to the overall average, despite spread within each tectonic
289 setting: MORB = +0.06±0.17 ‰ (2s, n=12); OIB = +0.06±0.24 ‰ (2s, n=13); and the Cameroon Line
290 samples = +0.08±0.06 ‰ (2s, n=15). Tanzanian nephelinites average a slightly heavier Ni isotope
291 composition ($\delta^{60/58}$Ni = +0.14±0.03 ‰, 2s, n=2).

292 **Table 1**

293 Ni concentration and isotopic composition of mafic samples

| Sample Code | Lithology | Locality | Ni (μg $g^{-1}$) | $\delta^{60/58}$Ni | 2s | n |
|---|---|---|---|---|---|---|
| **Mid Ocean Ridge Basalts** | | | | | | |
| R82-1 | N-MORB | East Pacific Ridge | 125.0 | +0.19 | 0.06 | 4 |
| R94-2 | N-MORB | East Pacific Ridge | 43.62 | +0.19 | 0.05 | 4 |
| R93-7 | E-MORB | East Pacific Ridge | 121.1 | +0.05 | 0.03 | 2 |
| A127 D5-5 | N-MORB | Mid Atlantic Ridge | 156.6 | +0.15 | 0.01 | 2 |
| A127 D8-2 | N-MORB | Mid Atlantic Ridge | 138.5 | +0.06 | 0.01 | 3 |
| A127 D10-2A | MORB | Mid Atlantic Ridge | 81.20 | +0.12 | 0.03 | 3 |
| A127 D15-1 | E-MORB | Mid Atlantic Ridge | 61.46 | +0.03 | 0.00 | 2 |
| A127 D17-3 | E-MORB | Mid Atlantic Ridge | 90.86 | -0.04 | 0.03 | 4 |
| A127 D21-3 | E-MORB | Mid Atlantic Ridge | 54.48 | -0.02 | 0.04 | 4 |
| A127 D22-5 | E-MORB | Mid Atlantic Ridge | 38.07 | +0.02 | 0.01 | 2 |
| A127 D26-5 | E-MORB | Mid Atlantic Ridge | 84.67 | -0.02 | 0.07 | 3 |
| A127 D27-5 | E-MORB | Mid Atlantic Ridge | 116.5 | -0.04 | 0.02 | 2 |
| **Ocean Island Basalts** | | | | | | |
| AZF3 | transitional basalt | Flores, Azores | 374.3 | -0.04 | 0.02 | 4 |
| AZFY2 | alkali basalt | Fayal, Azores | 167.4 | -0.11 | 0.07 | 3 |
| AZP6 | alkali basalt | Pico, Azores | 47.94 | -0.16 | 0.00 | 2 |
| PL02 25-1 | alkali basalt | Galápagos | 77.55 | -0.03 | 0.02 | 7 |
| PL02 30-1 | tholeiite | Galápagos | 118.4 | +0.01 | 0.07 | 2 |
| D4-6G | alkali basalt | Lō'ihi, seamount nr Hawaii | 238.5 | +0.17 | 0.06 | 7 |
| ST38 | tholeiite | Skaldsstaðir, N. Iceland | 86.00 | +0.19 | 0.06 | 4 |
| GS18 | tholeiite | Granastaðir, N. Iceland | 57.00 | +0.22 | 0.02 | 4 |
| CX11 | tholeiite | Hjaleigulaekur, E. Iceland | 49.48 | +0.23 | 0.03 | 4 |
| CX19 | tholeiite | Hjaleigulaekur, E. Iceland | 76.73 | +0.11 | 0.02 | 2 |
| SNB19 | tholeiite | Snaefellsnes, W. Iceland | 197.3 | +0.01 | 0.03 | 2 |
| SNB40 | tholeiite | Snaefellsnes, W. Iceland | 167.9 | +0.03 | 0.03 | 4 |
| SNB42 | tholeiite | Snaefellsnes, W. Iceland | 202.8 | +0.12 | 0.04 | 3 |
| **Cameroon Line** | | | | | | |
| P18 | olivine nephelinite | Príncipe, Island, Cameroon Line | 184.1 | +0.03 | 0.07 | 3 |
| C134 | mafic nephelinite | Etinde, Cameroon | 42.67 | +0.12 | 0.05 | 3 |
| C151 | mafic nephelinite | Etinde, Cameroon | 92.16 | +0.06 | 0.03 | 5 |
| C22 | nephelinite | Etinde, Cameroon | 12.58 | +0.08 | 0.04 | 6 |

| | | | | | | |
|---|---|---|---|---|---|---|
| C20 | nephelinite | Etinde, Cameroon | 12.17 | +0.07 | 0.04 | 4 |
| C152 | hauyne nephelinite | Etinde, Cameroon | 7.76 | +0.11 | 0.07 | 5 |
| C150 | olivine melanephelinite | Etinde, Cameroon | 43.04 | +0.07 | 0.08 | 6 |
| C65 | Hy-normative basalt | Manengouba, Cameroon | 228.2 | +0.06 | 0.04 | 3 |
| C192 | basanite | Mt Cameroon, Cameroon | 52.88 | +0.07 | 0.04 | 3 |
| C30 | basanite | Mt Cameroon, Cameroon | 213.8 | +0.11 | 0.01 | 3 |
| C112 | basanite | Bambouto, Cameroon | 133.9 | +0.10 | 0.02 | 3 |
| C51 | alkali basalt | Manengouba, Cameroon | 158.4 | +0.06 | 0.03 | 4 |
| C72 | alkali basalt | Manengouba, Cameroon | 150.8 | +0.07 | 0.07 | 2 |
| C146 | alkali basalt | Mandara Mts, Cameroon | 150.3 | +0.02 | 0.03 | 4 |
| FP44 | alkali basalt | Bioko, Island, Cameroon Line | 75.02 | +0.10 | 0.04 | 3 |
| **Continental Volcanism** | | | | | | |
| H93-3 | nephelinite | Kwaraha, N Tanzania | 149.2 | +0.16 | 0.05 | 3 |
| BD105 | olivine-melilite nephelinite | Oldoinyo, Loolmurwak, Tanzania | 359.3 | +0.13 | 0.06 | 3 |
| KH03-10L | basanite | Kilbourne Hole, USA | 151.5 | +0.127 | 0.02 | 2 |
| BD780 | ankaramite | Lashaine, Tanzania | 380.2 | +0.159 | 0.07 | 3 |

Ni concentration calculated by isotope dilution. n is the number of separate analyses of the sample. Samples analysed more than three times were also analysed from duplicate dissolutions. Intermediate precision of Ni isotope composition ±0.06 ‰.
Lithological designations from (Halliday et al., 1990; Halliday et al., 1992; Yi et al., 1995; Hardarson and Fitton, 1997; Niu and Batiza, 1997; Kempton et al., 2000; Harpp and White, 2001) as well as determination by the authors.
The MAR samples are sometimes referred to in the literature with AIII127 DR as prefix.

## 4.1 Mid ocean ridges

The MAR samples average $\delta^{60/58}$Ni = +0.03±0.13 ‰ (2s, n=9), whereas the EPR samples average +0.14±0.14 ‰ (2s, n=3). The 12 MORB samples can be divided on the basis of incompatible trace element ratios (specifically chondrite normalised La/Sm, e.g. Gale et al., 2013) into five N-MORB (normal, $La/Sm_N$ <1) and seven E-MORB (enriched, $La/Sm_N$ >1). Both N-MORB and E-MORB lithologies are included from each ridge analysed in this work. On average, N-MORB have heavier $\delta^{60/58}$Ni (+0.14±0.10 ‰, 2s, n=5) than E-MORB (+0.00±0.06 ‰, 2s, n=7), including both ridges. The average $\delta^{60/58}$Ni of MAR E-MORB (-0.01±0.05 ‰) is in agreement with the $\delta^{60/58}$Ni of the EPR E-MORB (+0.05 ‰); and average $\delta^{60/58}$Ni of MAR N-MORB (+0.11±0.08 ‰) are within error of EPR N-MORB (+0.19±0.00 ‰). One sample (A127 D10-8A) lacks published La and Sm data, but is assumed to be N-MORB, based on its heavier Ni isotope composition.

## 4.2 Ocean islands

The seven Icelandic samples average $\delta^{60/58}$Ni = +0.13±0.16 ‰ (2s). Two samples from Snaefellsnes have the lightest $\delta^{60/58}$Ni (SNB19 +0.01 ‰; SNB40 +0.03 ‰), and one further sample from this locality has $\delta^{60/58}$Ni = +0.12 ‰. The other four samples, from North and East Iceland, average +0.19±0.10 ‰ (2s).

The Azores samples have average $\delta^{60/58}$Ni = -0.10±0.10 ‰ (2s, n=3), which is the lightest $\delta^{60/58}$Ni of any mafic sample set. The $\delta^{60/58}$Ni of the samples vary from lightest $\delta^{60/58}$Ni (-0.16 ‰, Pico, alkali basalt) through mean $\delta^{60/58}$Ni composition (-0.11 ‰, Fayal, alkali basalt), to $\delta^{60/58}$Ni = -0.04 ‰ (Flores, transitional basalt) with geographical location from south-east (furthest from the MAR) to north-west (nearest ridge).

Of the remaining three OIB samples: the two Galápagos samples have average $\delta^{60/58}$Ni = -0.01±0.04 ‰ (2s), making this locality the second lightest on average for the OIB samples; and the single sample from Lō‘ihi seamount (alkali basalt) has a $\delta^{60/58}$Ni = +0.17 ‰.

### 4.3 Other intraplate mafic rocks

The Cameroon Line samples are identical in $\delta^{60/58}$Ni within analytical uncertainty. There is no resolvable difference between samples from the oceanic ($\delta^{60/58}$Ni = +0.07±0.07 ‰, 2s, n=2) and continental ($\delta^{60/58}$Ni = +0.08±0.05 ‰, 2s, n=13) sectors nor between lithologies: hypersthene-normative basalt ($\delta^{60/58}$Ni = +0.06‰, n=1), alkali basalts ($\delta^{60/58}$Ni = +0.06±0.06 ‰, 2s, n=4), basanites ($\delta^{60/58}$Ni = +0.09±0.04 ‰, 2s, n=3) and nephelinites ($\delta^{60/58}$Ni = +0.08±0.05 ‰, 2s, n=7). The $\delta^{60/58}$Ni of the Cameroon Line samples shows no relationship with MgO or Ni content (Figure 2). The samples that represent the lightest (+0.02 ‰, Mandara Mountains, alkali basalt) and heaviest (+0.12 ‰, Etinde, mafic nephelinite) $\delta^{60/58}$Ni extremes of this sample suite are the only samples in this work that have $K_2O/P_2O_5 < 1$, which has been used as an indicator of post-eruption subaerial alteration (Hauri, 1996). Radiogenic isotope systems in the Cameroon Line have limited variation (e.g. $\varepsilon^{143}$Nd ranges from 3.32 to 5.85, Table EA3), and have been used to infer only limited source heterogeneity.

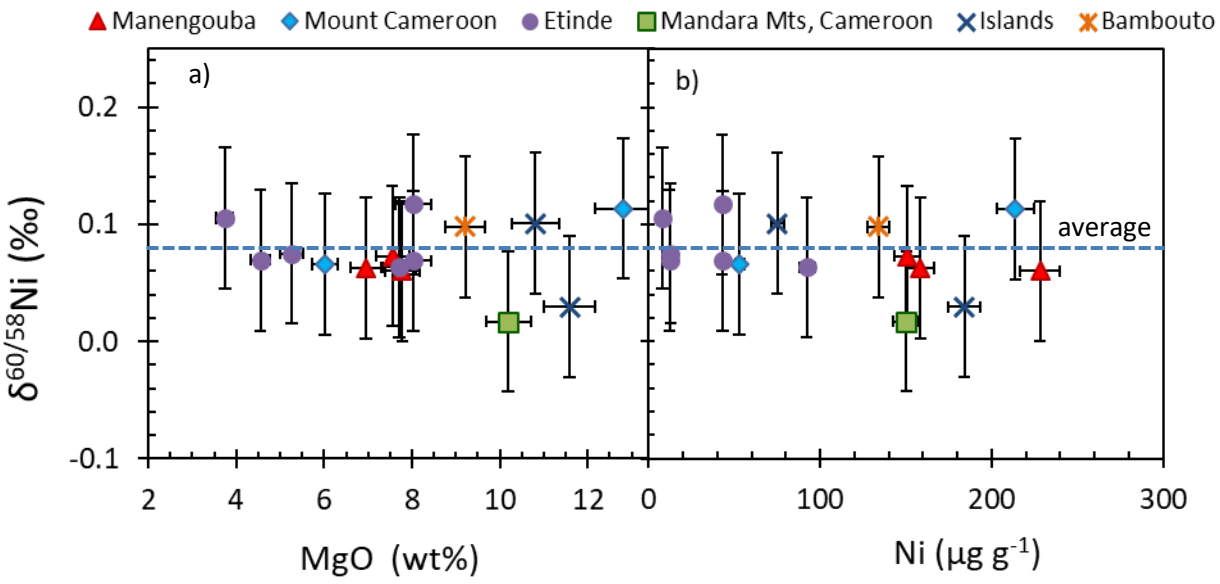


**Figure 2**

Nickel isotope composition in mafic rocks from the Cameroon Line:

a) Ni isotope composition vs MgO data from Fitton (2007)

b) Ni isotope composition vs Ni concentration as determined by isotope dilution.

No changes in Ni isotope composition are found with either MgO or Ni, even within any single volcanic system. Average mafic bulk rock Ni isotope composition for Cameroon Line rocks highlighted with blue dashed line at +0.08 ‰. Intermediate precision in Ni isotope composition is ±0.06 ‰.

The two nephelinite samples analysed from Tanzania have Ni isotope compositions within analytical uncertainty of each other (H93-3 = +0.16 ‰, BD105 = +0.13 ‰, analytical uncertainty = 0.06 ‰), and are isotopically heavier than the nephelinite samples of the Cameroon Line.

Similarly, the host basanite lava for Kilbourne Hole xenoliths has a Ni isotope composition of +0.13 ‰, and the host basanite (ankaramite) lava for the Lashaine xenoliths has a Ni isotope composition of +0.16 ‰.

# 5 Discussion

## 5.1 Lack of control on Ni isotope composition by tectonic setting

Samples from different tectonic settings (mid-ocean ridges, ocean islands, and the other intraplate volcanism) analysed in this study have indistinguishable mean Ni isotope compositions. These compositions are also within analytical uncertainty of the mean of the complete dataset (+0.07±0.17 ‰, 2s, n=44). This provides strong evidence that tectonic setting is not exerting a systematic control on Ni isotope composition.

The two geographically separate ridges overlap in MORB $\delta^{60/58}$Ni (MAR: -0.04 ‰ to +0.15 ‰; EPR: +0.05 ‰ to +0.19 ‰). For each ridge, E-MORB compositions have lighter Ni isotope compositions than N-MORB. These comparable patterns in Ni isotope compositions provide evidence that bulk rock $\delta^{60/58}$Ni is not affected by different spreading rates and proximity to mantle plumes, as sampling of the same ridge shows variation in Ni isotope compositions.

Heterogeneity in $\delta^{60/58}$Ni of ocean island basalts (-0.16 ‰ to +0.23 ‰) exceeds that observed in MORB in this work (-0.04 ‰ to +0.19 ‰). The range in Iceland (+0.01 ‰ to +0.23 ‰) is comparable to the entire range in MORB. Hawaii, using literature data from Kīlauea Iki (Wang et al., 2021), in addition to the Lo'ihi sample in Gueguen et al. (2013) and the Lo'ihi sample in this work, shows similar heterogeneity: $\delta^{60/58}$Ni ranges from -0.06 ‰ to +0.17 ‰. Such Ni isotope heterogeneity within a single plume provides evidence that factors such as proximity to a ridge are not a dominant control on the $\delta^{60/58}$Ni of the resulting OIB.

## 5.2 Processes that cannot explain heterogeneous mantle $\delta^{60/58}$Ni

### *5.2.1 Influence of partial melting and crystal fractionation*

Cameroon Line lithologies vary from hypersthene-normative basalt through alkali basalt to basanites and nephelinites (Figures 2, 3, EA1, EA2). These lithologies represent a range in silica saturation, produced by different degrees of partial melting, but have $\delta^{60/58}$Ni that are identical within error. This constant Ni isotope composition provides evidence that the effect of partial melting on $\delta^{60/58}$Ni is negligible. This is further supported by specific geochemical ratios such as Nb/Zr, which vary with degree of melting and show large variation in Cameroon Line samples but no correlation with Ni isotope composition (Figures EA1e, f).

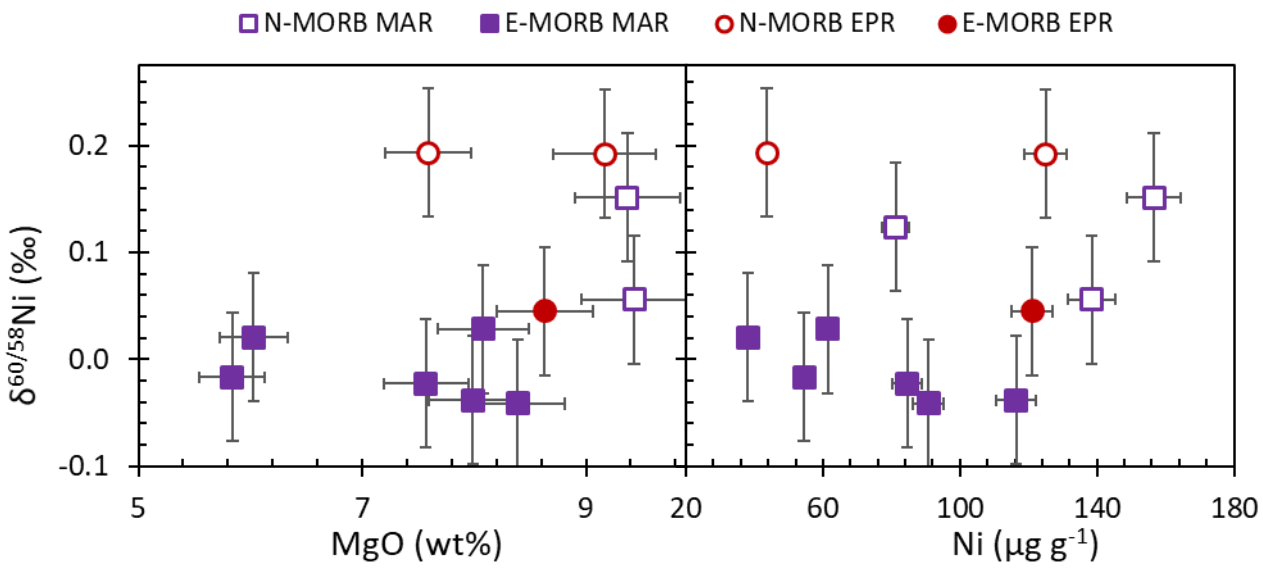


370

371 **Figure 3**

372 Nickel isotope composition for MORB plotted against MgO (where available) and Ni concentration. There is no correlation with
373 either, providing evidence that Ni isotope composition does not vary with fractional crystallisation. Data for MgO from Yi et al.
374 (2000) and Niu and Batiza (1997). Ni concentration is measured by isotope dilution by MC-ICPMS. Intermediate precision on the Ni
375 isotope compositions is ±0.06 ‰.

376

377 Additionally, MORB samples show no correlation between $\delta^{60/58}$Ni and $Na_{8.0}$ (Figure 4), which is also an
378 indicator of degree of partial melting and independent of fractional crystallisation (Klein and Langmuir,
379 1987). Sodium behaves as a moderately incompatible trace element at MORB melting conditions, with
380 highest concentrations at the smallest extents of melting, decreasing in concentration by dilution as the
381 extent of melting increases. To quantify this, $Na_{8.0}$ is calculated from the $Na_2O$ content at MgO = 8 wt.%,
382 correcting the sodium content for variations from fractional crystallization. Variation in $Na_{8.0}$ theoretically
383 only results from degree of partial melting (Klein and Langmuir, 1987). The lack of correlation between
384 $\delta^{60/58}$Ni and $Na_{8.0}$ provides further evidence that degree of melting does not affect Ni isotope compositions.

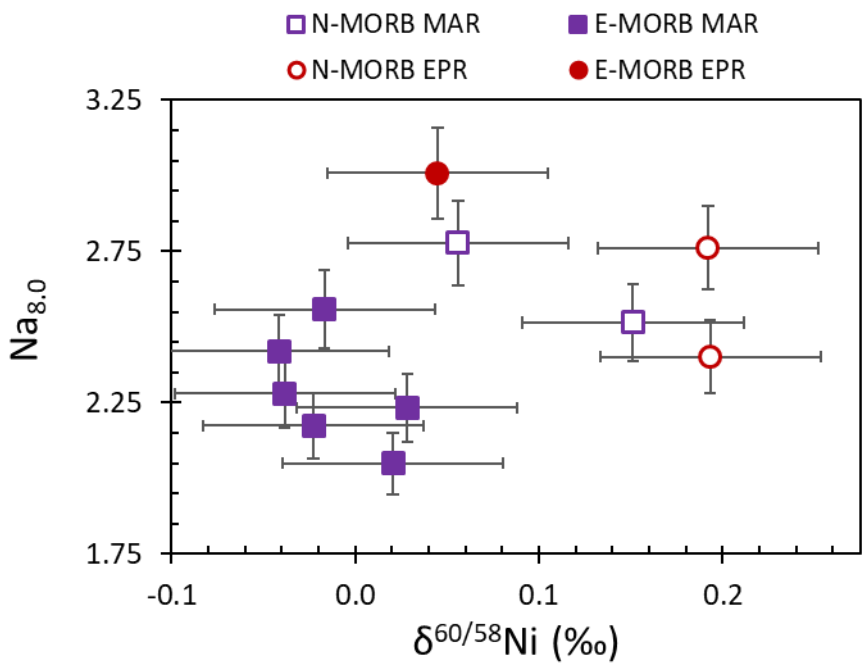


**Figure 4**

Nickel isotope composition for MORB plotted against $Na_{8.0}$, calculated by Na8.0 = Na20 + (0.373*(MgO)) - 2.98 as in Klein and Langmuir (1987). The lack of correlation provides further evidence that there is no relationship between Ni isotope compositions and degree of partial melting. Data for $Na_2O$ and MgO, where available, from Yi et al. (2000) and Niu and Batiza (1997). Intermediate precision on the Ni isotope compositions is ±0.06 ‰.

The host lavas for two xenolith sites analysed in Saunders et al. (2020) have been analysed. For Lashaine, the peridotite xenoliths average $\delta^{60/58}$Ni = +0.16±0.12 ‰ (2s, n=4, Saunders et al., 2020), and the host lava, an ankaramitic basanite, has identical $\delta^{60/58}$Ni of +0.16±0.07 ‰. For Kilbourne Hole the average peridotite xenolith $\delta^{60/58}$Ni = 0.16±0.14 ‰ (2s, n=15, Saunders et al., 2020), whereas the host lava, also a basanite, has a $\delta^{60/58}$Ni of +0.13±0.06 ‰. In both cases the mafic sample has a Ni isotope composition within error of the xenolith average. While not all xenoliths can be proven to be genetically linked to the mafic host, this coincidence in Ni isotope composition is suggestive that melting has not fractionated $\delta^{60/58}$Ni.

Variations in both MgO and Ni content in mafic magmas are dominantly controlled by olivine fractionation, as discussed in the Introduction. The relationship between these is presented in Figure EA2 for the Cameroon Line and MORB datasets. Although fractional crystallisation exerts a strong control on Ni concentration in mafic magmas, neither MgO nor Ni concentrations show any correlation with $\delta^{60/58}$Ni in intraplate samples from the Cameroon Line (n=15, Figure 2) or in MORB (n=12, Figure 3).

There are too few samples from any single OIB setting to unambiguously show that there is no significant $\delta^{60/58}$Ni fractionation associated with crystal fractionation. However, there is no obvious reason why processes in ocean island tectonic settings would fractionate Ni isotopes in a manner not observed in the Cameroon Line basaltic lavas or in MORB.

The conclusion that $\delta^{60/58}$Ni is not significantly fractionated by melting or fractional crystallisation is in agreement with modelling which found no change in mantle restite $\delta^{60/58}$Ni even with large degrees of melting (Klaver et al., 2020). Klaver et al. (2020) suggest up to 0.15 ‰ as the maximum fractionation during melting of the mantle for which residual $\delta^{60/58}$Ni would be buffered at a constant composition. This work has shown that $\delta^{60/58}$Ni in mafic rocks far exceeds this limit yet the corresponding fractionation in peridotites were this to result from melting is not observed in literature data (Klaver et al., 2020; Saunders et al., 2020; Wang et al., 2021).

### *5.2.2 Core entrainment*

Leakage of material from the core with a Ni isotope composition distinct from the mantle, could be entrained into mantle plumes by mantle convection. Entrainment of core material, which contains approximately 5 % Ni (Clement et al., 1997), has been invoked to explain $^{182}$W heterogeneity (Rizo et al., 2019), iron isotope heterogeneity (Liu et al., 2017; Lesher et al., 2020), and primordial He ratios (Jackson et al., 2017) in some ocean island basalt samples. If the core had a different $\delta^{60/58}$Ni to the bulk mantle, this signal could potentially be present in mantle-derived rocks, producing isotopic heterogeneity. Material entrained from the outer core would also contain ~80 wt% Fe (Clement et al., 1997), therefore any mantle heterogeneity in Ni isotope composition introduced from the core would be expected to be associated with higher than normal iron content.

Recent studies including mass balance of chondrite and peridotite compositions (Klaver et al., 2020; Wang et al., 2021) provide evidence that core metal would be isotopically heavier than the BSE; and experimental petrology and ab initio calculations (Guignard et al., 2020), provide evidence that negligible Ni isotope fractionation would be observed between core and mantle at the conditions of the core-mantle boundary. The $\delta^{60/58}$Ni heterogeneity in the mantle extends from unmetasomatised peridotite (~$\delta^{60/58}$Ni = +0.20 ‰) to lighter compositions, indicating that core derived material, which is predicted to have, if any difference, heavier

than BSE $\delta^{60/58}$Ni, can not be reponsible for the observed variation. Core material with an unfractionated Ni isotope composition, as predicted by Guignard et al. (2020) and Wang et al. (2020) could not induce an observable heterogeneity in mantle materials.

Further, Figures 5 and 6 show that isotopically light Ni in MORB is also associated with enrichment in La/Sm, Rb/Sr etc. Such incompatible (Hofmann, 1997) and lithophile elements (Wood et al., 2019) are not present in the outer core in amounts that could explain the observed trends. This provides further evidence that core entrainment is unlikely to contribute to the observed $\delta^{60/58}$Ni heterogeneity in the mantle and mantle-dervied mafic rocks. This does not rule out the possibility of core entrainment role if future studies extend the observed mantle heterogeneity to significantly heavier $\delta^{60/58}$Ni values.

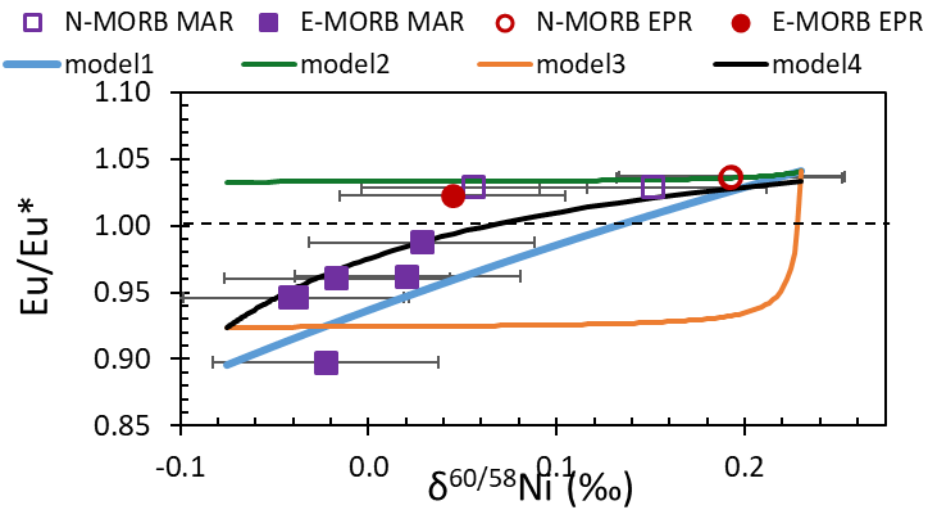


**Figure 5**

A plot of Eu anomaly (Eu/Eu*, calculated as the ratio of the difference between chondrite normalised (McDonough and Sun, 1995) Eu concentration and the mean of the magnitudes of chondrite normalised Gd and Sm concentrations for that sample) against Ni isotope composition for MORB samples defines a hyperbolic mixing relationship between two endmember compositions. Data for Eu, Gd, & Sm, (where available) from Yi et al. (2000) and Niu and Batiza (1997). Intermediate precision on the Ni isotope compositions is ±0.06 ‰. Mixing lines each have one endmember with $\delta^{60/58}$Ni = +0.23 ‰ and the other with $\delta^{60/58}$Ni = -0.075 ‰. Model1 is a best fit with DMM (Workman and Hart, 2005) as one endmember, and the other chosen to reproduce the data array. This model has the enriched endmember with light $\delta^{60/58}$Ni and lower [Ni] than the depleted mantle. Model2 uses DMM as one endmember, and the other an average pyroxenite composition from Saunders et al. (2020) and Xu (2002). Model3 uses DMM as one endmember and average kimberlite composition (Le Roex et al., 2003) as the other. Model4 uses DMORB (Gale et al., 2013) as one endmember, and average kimberlite composition as the other. Model4 comes closest to replicating the sense of curvature of the array (Model1).

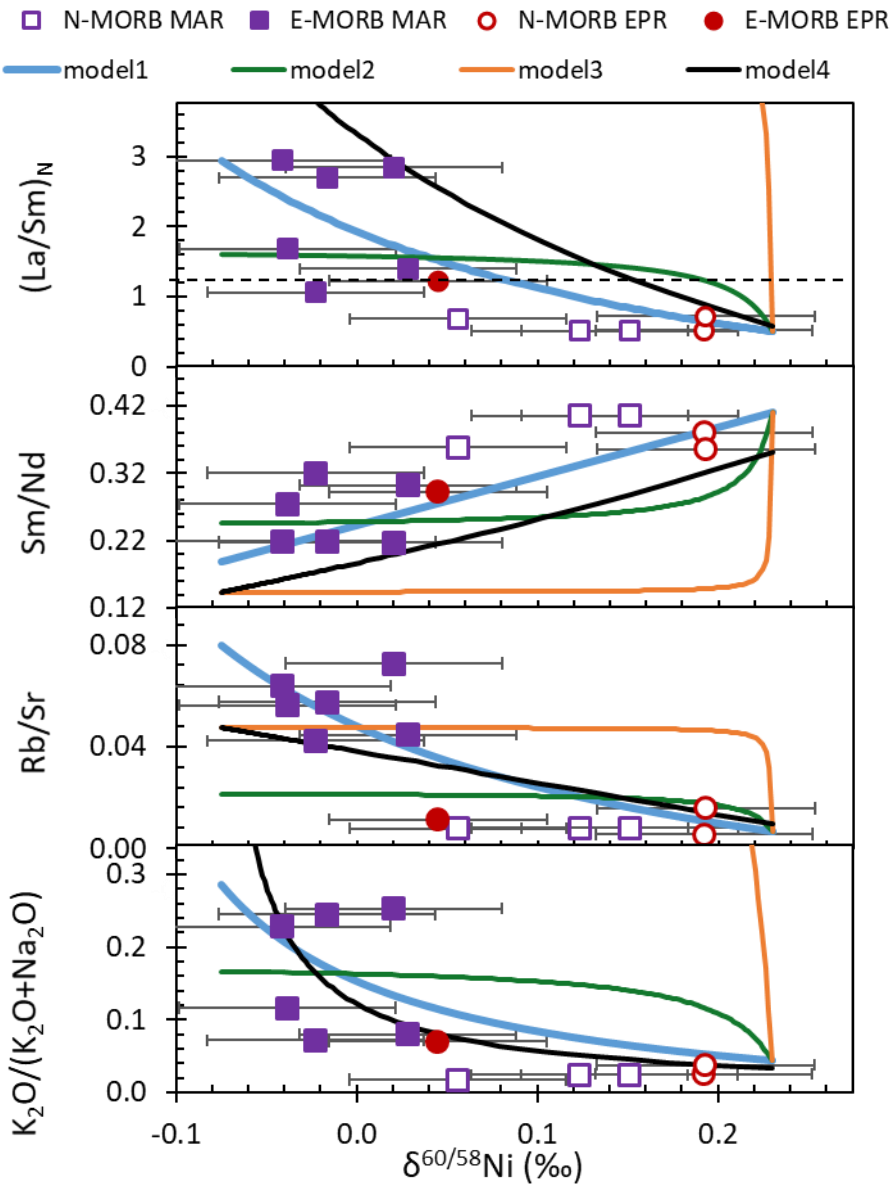


**Figure 6**

Large-ion lithophile element ratios plotted against Ni isotope composition for MORB. Circles: East Pacific Rise; squares: Mid Atlantic Ridge, with E-MORB shown by open symbols and N-MORB by solid symbols. All show a potentially hyperbolic mixing relationship between two endmember compositions. Data for La, Sm, Rb, Sr, Yb, $K_2O$, and $Na_2O$ (where available) from Yi et al. (2000) and Niu and Batiza (1997). CI chondrite composition from McDonough and Sun (1995). The separation in Ni isotope composition of E-MORB and N-MORB, as defined by $(La/Sm)_N$ (chondrite normalised) is clear, and supports a mixing hypothesis in the mantle source. Intermediate precision on the Ni isotope compositions is ±0.06 ‰. Mixing lines each have one endmember with $\delta^{60/58}Ni$ = +0.23 ‰ and the other with $\delta^{60/58}Ni$ = -0.075 ‰. Model1 is a best fit with DMM (Workman and Hart, 2005) as one endmember, and the other chosen to reproduce the data array. This model has the enriched endmember with light $\delta^{60/58}Ni$ and lower [Ni] than the depleted mantle. Model2 uses DMM as one endmember, and the other an average pyroxenite composition from Saunders et al. (2020) and Xu (2002). Model3 uses DMM as one endmember and average kimberlite composition (Le Roex et al., 2003) as the other. Model4 uses DMORB (Gale et al., 2013) as one endmember, and average kimberlite composition as the other. Model4 comes closest to replicating the sense of curvature of the array (Model1).

## 5.3 Potential recycling signatures in Ni isotope composition of mafic rocks

A relationship between isotopically light $\delta^{60/58}$Ni and mantle enrichment from recycled material has been previously proposed, based on the association of light $\delta^{60/58}$Ni with unradiogenic $\varepsilon^{143}$Nd in mantle xenoliths from Kilbourne Hole, New Mexico (Saunders et al., 2020). Mantle enrichment is characterised by enriched radiogenic isotope signatures relative to the depleted MORB mantle, such as less radiogenic Nd isotopic compositions (e.g. Zindler and Hart, 1986; Haase et al., 2011). Possible enrichment processes include recycling of oceanic crust and sediment via subduction, and this material can then be entrained in mantle plumes and returned to the surface in oceanic basalts (e.g. Hofmann and White, 1982; Pearson and Nowell, 2004). As $\delta^{60/58}$Ni is heterogeneous in mafic samples but also unaffected by tectonic setting, partial melting and fractional crystallisation, a recycling signature could be preserved in these samples.

Variations in radiogenic isotope ratios, such as $^{143}$Nd/$^{144}$Nd, result from differences in parent / daughter ratios and time. Since mantle enrichment can result from a variety of recycled materials and processes and at different times over Earth's history, relationships between $\delta^{60/58}$Ni and Nd isotope compositions, or any other radiogenic signal, are expected to be site specific. The radiogenic isotope ratios in the mafic samples in this study have a limited range; for example, Nd isotope compositions range from $\varepsilon^{143}$Nd =2.3 to 10.0, see Table EA3. Therefore, the $\delta^{60/58}$Ni in this sample set do not include representatives of the most extreme enriched mantle compositions sampled in OIB. Neodymium isotopic ratios have been measured on only five of the MAR samples, all of which were E-type tholeiites, and had $\delta^{60/58}$Ni values identical within the intermediate precision of this study. The limited Nd isotopic data on any single volcanic system analysed for $\delta^{60/58}$Ni in the present study, also limits comparison with the $\delta^{60/58}$Ni and Nd isotope data available for the ultramafic samples from Kilbourne Hole. However, the connection between $\delta^{60/58}$Ni and indicators of recycling can be shown with other indicators.

The average $\delta^{60/58}$Ni for E-MORB samples from both MAR and EPR, shows almost no overlap with a heavier average N-MORB $\delta^{60/58}$Ni, which strongly supports an enriched component being associated with lighter $\delta^{60/58}$Ni. Figures 5 and 6 also show that the $\delta^{60/58}$Ni of E-MORB and N-MORB (as defined by $(La/Sm)_N < 1$, where N represents normalisation to CI chondrite composition (McDonough and Sun, 1995)) is a continuum, such as would be expected for mafic rocks forming from an isotopically heterogeneous source.

Figure 6 shows that lighter Ni isotope compositions ($\delta^{60/58}$Ni < 0.00 ‰) in MORB are also associated with high Rb/Sr, low Sm/Nd, and high $K_2O/(K_2O+Na_2O)$. Light $\delta^{60/58}$Ni is additionally associated with negative Eu anomalies (an Eu concentration less than that interpolated from a normalised REE concentration plot, see Figure 5). The MORB data arrays in Figures 5 and 6 form a continuum from $\delta^{60/58}$Ni ~ +0.05 ‰, Eu/Eu* ~0.88 and $(La/Sm)_N$ >1 to $\delta^{60/58}$Ni ~ +0.20 ‰, Eu/Eu* ~1.04 and $(La/Sm)_N$ < 1; strongly supporting an interpretation based on mixing between an enriched light $\delta^{60/58}$Ni end-member and a depleted one with heavier $\delta^{60/58}$Ni.

The lightest Ni isotope compositions in mafic rocks reported here have been observed in basalts from the Azores ($\delta^{60/58}$Ni = -0.04 ‰ from Flores, -0.11 ‰ from Fayal, -0.16 ‰ from Pico). The Azores magmas have been inferred either to contain a component from recycled sediment (Hawkesworth et al., 1979) or to have contributions from localized domains of recycled lithospheric mantle entrained within the plume (Widom and Shirey, 1996; Schaefer et al., 2002). The most extreme unradiogenic Os isotope compositions, associated with recycled crustal material, have been observed at Pico and Fayal (Schaefer et al., 2002), where the lightest $\delta^{60/58}$Ni compositions from this mafic sample suite are observed. These observations that support an enriched recycled component in the Azores plume provide further evidence that light $\delta^{60/58}$Ni compositions may be related to enriched mantle and can be sampled by mafic rocks and some ultramafic samples.

The relationships observed in MORB $\delta^{60/58}$Ni in Figures 5 and 6 were explored with simple mixing models. In the first, one endmember was the depleted MORB mantle (DMM) of Workman and Hart (2005) with $\delta^{60/58}$Ni at the heavier end of BSE estimates (+0.23 ‰). The other endmember was designed to provide a best fit to the data with enriched elemental concentrations and $\delta^{60/58}$Ni at the lightest published peridotite compositions (specifically, -0.075 ‰). The elemental input values can be found in Table EA4, with 'model1' being our preferred fit to the data. The enriched endmember composition of this preferred model has a Ni concentration comparable to Ni-rich kimberlites / pyroxenites, but lower than the Ni concentration of DMM, and has a higher K concentration (Table EA4). Using DMM with admixed pyroxenite (model2, data from Xu 2002; Saunders et al., 2020) and kimberlite (model3, data from Le Roex et al., 2003), yields mixing lines with the opposite sense of curvature. Model4 uses kimberlite for the enriched composition and D-MORB for the depleted endmember. This model comes closest to replicating the best fit trends.

The model is purely illustrative of the kinds of mixing relationships that might be responsible for the MORB $\delta^{60/58}$Ni variability but which require more detailed study. The OIB samples do not fit with the MORB data array, therefore model endmember compositions tested here cannot reproduce all of the analysed mafic compositions reported. Further work is required to establish if accurate lithological endmembers will be able to reproduce the available $\delta^{60/58}$Ni data under realistic mantle mixing conditions.

While the endmember composition with light $\delta^{60/58}$Ni is hypothetical in model1, numerous lithologies have been observed to have light $\delta^{60/58}$Ni in published work (Figure EA3). These include eclogites (Wang et al., 2021), which form during subduction and have an average $\delta^{60/58}$Ni of +0.03±0.06 ‰ (2s, n=7). Eclogites also show significant variability in trace element composition (Zhang et al., 2013). Additionally, $\delta^{60/58}$Ni lighter than that of eclogites is observed in organic rich shales (Pašava et al., 2019); some sulphides and sulphidic rocks (Gueguen et al., 2013; Hofmann et al., 2014); and many materials formed from low temperature surface processes. The latter group include soils (Ratié et al., 2015; Ratié et al., 2016; Ratié et al., 2019); lacustrine shales (Li et al., 2021); diamictites (Wang et al., 2019); saprolites (Ratié et al., 2015); and serpentinites (Gueguen et al., 2013). Serpentinites form a large part of subducted oceanic lithosphere (e.g. Bach et al., 2004; Paulick et al., 2006); and contributions from sulphidic material, common in euxinic ocean conditions, and often enriched in Ni, cannot be discounted. Additionally, pronounced negative Eu anomalies are especially characteristic of shales, loess, and granites (Niu and O'Hara, 2009); which could contribute to the negative Eu anomalies observed in MORB with lighter $\delta^{60/58}$Ni. Further, the processes that produce fractionations to lighter $\delta^{60/58}$Ni in surface environments, as observed in terrestrial material, may well be replicated in ocean basins, and fractionate material before subduction. Available evidence cannot exclude $\delta^{60/58}$Ni fractionation during subduction as another possibility.

Additionally, elevated Rb/Sr, lower Sm/Nd, and higher K, each associated with lighter $\delta^{60/58}$Ni in MORB, are also geochemical characteristics of arc magmas (Volpe et al., 1987). Arc magmas can also have negative Eu anomalies, such as observed in MORB with lighter $\delta^{60/58}$Ni, (Eu/Eu* > 0.8; Niu and O'Hara, 2009). Arc magmas are formed at subduction zones, therefore recycled material can produce mantle sources that have the same characteristics as associated with light $\delta^{60/58}$Ni in this work. Similarly, elevated Rb/Sr and lower Sm/Nd than depleted MORB are characteristics of E-DMM (Workman and Hart, 2005), a hypothetical

551 mantle composition calculated as being more enriched than the average composition of plume-distant
552 MORB by 2× standard deviation on the concentration of each element. This is consistent with the hypothesis
553 that geochemical signatures that correlate with lighter $\delta^{60/58}$Ni are associated with recycled input to the
554 mantle. Additionally, lighter $\delta^{60/58}$Ni in clinopyroxene separates from ultramafic xenoliths was previously
555 also observed to correlate strongly with higher La/Sm, and lower Sm/Nd of the host rock (data from
556 Saunders et al., 2020), comparable to the trend in MORB samples (Figure EA4). Inter-mineral fractionation
557 in ultramafic xenoliths is small, but varies with the bulk rock composition and the mineral chemistry,
558 therefore influencing Ni isotope compositions at some finite level. It seems likely that further work on this
559 subject will be needed to fully explain these observations.

560 The present work provides substantial evidence that the $\delta^{60/58}$Ni of mafic rocks directly reflects the $\delta^{60/58}$Ni of
561 their mantle source. Lighter $\delta^{60/58}$Ni domains may be transported by physical mixing on long timescales, with
562 the $\delta^{60/58}$Ni remaining unchanged by time, mantle melting or differentiation, and subsequently entrained in
563 the upper mantle to contribute to mantle sources of mafic rocks. Nickel isotope compositions, therefore,
564 could provide an ideal new tracer for mantle mixing of recycled material back into heterogeneously melt-
565 depleted residual mantle.

566

567 **5.4 Nickel isotopes and the bulk silicate Earth (BSE)**

568 Early estimates of $\delta^{60/58}$Ni in the BSE were calculated from a limited number of ultramafic samples; mostly
569 geochemical reference materials. These early estimates for Ni isotope composition of the BSE are
570 indistinguishable from each other at the 2σ level: $\delta^{60/58}$Ni = +0.18±0.04 ‰ (Steele et al., 2011); $\delta^{60/58}$Ni =
571 +0.23±0.06 ‰ (Gall et al., 2017). Further estimates based on peridotite data are significantly lower and also
572 in close agreement with each other: $\delta^{60/58}$Ni = +0.11±0.01 ‰ (Elliott and Steele, 2017, using data from
573 Gueguen et al., 2013), $\delta^{60/58}$Ni = +0.12±0.05 ‰ (Klaver et al., 2020), and $\delta^{60/58}$Ni = +0.11±0.07 ‰ (Wang et
574 al. (2021), using additional data from Klaver et al. (2020)). This range suggests that peridotite sample
575 selection greatly influences the resulting BSE average Ni isotope composition.

576 Recent work has provided evidence that individual peridotite samples exhibit wider ranges in $\delta^{60/58}$Ni than
577 are expected to be produced by high-temperature non-redox-sensitive processes. Ranges in peridotite $\delta^{60/58}$Ni

578 of +0.04 ‰ to +0.22 ‰, (n=24, Klaver et al., 2020), +0.02 ‰ to +0.26 ‰ (n=24, Saunders et al., 2020), and
579 -0.08 ‰ to +0.20 ‰ (n=33, Wang et al, 2021) have greatly extended the previously published dataset.
580 Earlier data of four massif peridotites (range +0.26 ‰ to +0.32 ‰, Ratie et al., 2015) add heavier
581 compositions to the data range, comparable to the seven heavier compositions observed for ultramafic
582 xenoliths in Gall (2017), which ranged from +0.18 ‰ to +0.36 ‰. These data provide evidence of
583 considerable $\delta^{60/58}$Ni heterogeneity in the mantle sampled by peridotites. Cryptic metasomatism has been
584 shown to not be a dominant cause of heterogeneity in $\delta^{60/58}$Ni as metasomatised examples of spinel
585 lherzolites and harzburgites ($\delta^{60/58}$Ni = -0.08 ‰ to +0.23 ‰) have comparable ranges to unmetasomatised
586 (+0.04 ‰ to +0.26 ‰) samples of those lithologies (Klaver et al., 2020; Saunders et al., 2020; Wang et al.,
587 2021). Pyroxenite xenoliths have wider ranges in $\delta^{60/58}$Ni than peridotites, with lighter $\delta^{60/58}$Ni associated
588 with mantle fertility and enrichment (Saunders et al., 2020).

589 These wide variations in $\delta^{60/58}$Ni of the ultramafic sample set (average +0.13±0.20 ‰, 2s, n=98) raise doubts
590 as to the potential for a simple mean of any ultramafic subset of samples to be truly representative of the
591 terrestrial mantle. Even an average of all published samples may not be representing the volumetric
592 contributions of some observed extremes in $\delta^{60/58}$Ni.

593 The present study has shown that $\delta^{60/58}$Ni heterogeneity in mafic samples (-0.16 ‰ to +0.23 ‰) is
594 comparable in range to that observed in peridotite samples. Furthermore, we have provided evidence that Ni
595 isotopes are unfractionated by partial melting and fractional crystallisation. Therefore, because mafic rocks
596 are formed by the partial melting of large regions of the mantle, these samples could provide an estimate of
597 the average $\delta^{60/58}$Ni composition for a greater volume of the mantle than any set of ultramafic samples. The
598 larger region of mantle sampled by mafic magma would additionally give any input from the extremes of
599 $\delta^{60/58}$Ni, as observed in some non-peridotitic ultramafic lithologies, a more proportionate contribution.
600 Further, the similar averages in $\delta^{60/58}$Ni for each tectonic setting analysed here (Figure 1) provide evidence
601 that any suite of mafic samples represents a reproducible average $\delta^{60/58}$Ni composition, for the bulk mantle.

602 Therefore, an average for a suite of mafic samples could be used as a BSE estimate, and eliminate the
603 uncertainty represented by the relative sensitivity of sample selection associated with BSE estimates from
604 bulk rock peridotites. The resulting composition of the BSE by this method (e.g. $\delta^{60/58}$Ni = +0.08±0.06 ‰, to

use the Cameroon line example), agrees with recent arguments for a sub-chondritic BSE $\delta^{60/58}$Ni (+0.12±0.05 ‰, Klaver et al., 2020; +0.11±0.06 ‰ Wang et al., 2021), which strongly suggests that the Ni isotope composition in basalts is, on average, dominated by average mantle, despite the very light $\delta^{60/58}$Ni found in, for example, some pyroxenite lithologies. The average $\delta^{60/58}$Ni of the mafic samples is also within analytical uncertainty of the average of peridotite $\delta^{60/58}$Ni of +0.14 ± 0.15 ‰ (2s, n=93, Ratié et al., 2015; Gall et al., 2017; Klaver et al., 2020; Saunders et al., 2020; Wang et al., 2021).

## 6 Conclusions

The wide range of $\delta^{60/58}$Ni reported here provides further evidence of significant heterogeneity in $\delta^{60/58}$Ni in the mantle, and evidence that the process responsible for heterogeneous Ni isotopes in the mantle must be ubiquitous and highly variable. Nickel isotope compositions in mafic samples do not vary systematically with tectonic setting, degree of partial melting or fractional crystallisation. With Ni isotopes unmodified by these factors, the $\delta^{60/58}$Ni composition of mafic rocks reflects that of their specific mantle source region of the volcanic system.

The conclusion of Saunders et al. (2020) that lighter $\delta^{60/58}$Ni is associated with mantle enrichment is further supported by the present study, with E-MORB having lighter $\delta^{60/58}$Ni and higher chondrite-normalised La/Sm. The lighter $\delta^{60/58}$Ni in E-MORB to heavier $\delta^{60/58}$Ni in N-MORB relationship is evident in both MAR and EPR samples. The correlation forms a continuum, similar to that defined by $\delta^{60/58}$Ni and $\varepsilon^{143}$Nd in Kilbourne Hole ultramafic xenoliths. The enrichment trend from heavier $\delta^{60/58}$Ni in N-MORB to lighter $\delta^{60/58}$Ni in E-MORB correlates with an enrichment in lithophile elements that cannot be added to the mantle from entrainment of outer core material, reducing the likelihood that this process might be the origin of the observed trends. The relationships between MORB $\delta^{60/58}$Ni and these geochemical indicators of enrichment can be reproduced by a simple mixing model, although the enriched endmember composition has not been matched to a specific lithology. However, an enriched endmember is consistent with enriched mantle lithologies that have strong associations with light $\delta^{60/58}$Ni observed in pyroxenite xenoliths from Kilbourne Hole and Cameroon (Saunders et al., 2020). Nickel isotope composition is unaffected by the time elapsed since the input of recycled material, unlike radiogenic isotope systems. Nickel isotopes, therefore, have the

potential to quantify the amount of enriched recycled component regardless of the time since $\delta^{60/58}$Ni fractionation and the incorporation of that material into the mantle source.

Each mantle source region has a Ni isotope composition that we suggest is controlled by the amount of recycled enriched material incorporated into that region. Mafic rocks represent the Ni isotope composition of large volumes of the mantle. The average composition of mafic rocks from any given tectonic setting (OIB, MORB, and intraplate) is identical, suggesting that mafic sample sets can produce a reproducible estimate of Bulk Silicate Earth Ni isotope composition. The $\delta^{60/58}$Ni average of all ultramafic samples published to date (+0.13±0.20 ‰, 2s, n=98), is within analytical uncertainty of the most recent BSE $\delta^{60/58}$Ni estimates (+0.12±0.05 ‰, Klaver et al., 2020; +0.11±0.06 ‰, Wang et al., 2021), but due to the wide range of $\delta^{60/58}$Ni observed, may not be volumetrically representative of the actual BSE. Given the lack of fractionation in Ni isotopes with melting, a more accurate bulk mantle composition may be obtained from an average of a mafic sample suite, as each tectonic setting reproduces the same mean. Therefore, the Cameroon Line $\delta^{60/58}$Ni average (+0.08±0.06 ‰) may be used as a BSE estimate, as valid as the average of the entire mafic sample set of this work ($\delta^{60/58}$Ni = +0.07±0.17 ‰).

## Acknowledgements

This work was supported by an STFC PhD studentship (1508639) awarded to NJS through a grant awarded to ANH (Planetary Origins and Developments: ST/M001318/1) by the Science and Technology Facilities Council (STFC), and by funds from both Oxford and Columbia Universities. MC-ICPMS analyses were aided by Yu-Te Alan Hsieh; ICPMS analyses by Philip Holdship. The African continental samples used in this study were either collected by JGF or during fieldwork carried out by teams including ANH. Icelandic samples collected by Björn Hardarson provided via JGF and ANH. Other basalt samples are from the collection of ANH.

# References


Atouba L. C. O., Chazot G., Moundi A., Agranier A., Bellon H., Nonnotte P., Nzenti J. P. and Kankeu B. (2016) Mantle sources beneath the Cameroon Volcanic Line: geochemistry and geochronology of the Bamoun plateau mafic rocks. *Arab. J. Geosci.* **9**.

Bach W., Garrido C. J., Paulick H., Harvey J. and Rosner M. (2004) Seawater-peridotite interactions: First insights from ODP Leg 209, MAR 15°N. *Geochemistry, Geophys. Geosystems* **5**, 9–26.

Beier C., Haase K. M. and Turner S. P. (2012) Conditions of melting beneath the Azores. *Lithos* **144**–**145**, 1–11.

Cameron V., Vance D., Archer C. and House C. H. (2009) A biomarker based on the stable isotopes of nickel. *Proc. Natl. Acad. Sci.* **106**, 10944–10948.

Clement B. M., Holzheid A. and Tilgner A. (1997) Core geophysics. *Proc. Natl. Acad. Sci. U. S. A.* **94**, 12742–12743.

Dawson J. B. (2012) Nephelinite-melilitite-carbonatite relationships: Evidence from Pleistocene-recent volcanism in northern Tanzania. *Lithos* **152**, 3–10.

Dawson J. B. and Smith J. V. (1988) Metasomatised and veined upper-mantle xenoliths from Pello Hill, Tanzania: evidence for anomalously-light mantle beneath the Tanzanian sector of the East African Rift Valley. *Contrib. Mineral. Petrol.* **100**, 510–527.

Dosso L., Bougault H., Langmuir C., Bollinger C., Bonnier O., Etoubleau J. (1999) The age and distribution of mantle heterogeneity along the Mid-Atlantic ridge (31-41°N). *Earth Planet. Sci. Lett.* **170**, 269–286.

Elliott T. and Steele R. C. J. (2017) The Isotope Geochemistry of Ni. In *Reviews in Mineralogy & Geochemistry*

Fitton J. G. (1987) The Cameroon line, West Africa: a comparison between oceanic and continental alkaline volcanism. In *Alkaline Igneous Rocks, Geological Society Special Publications No. 30* pp. 273–291.

Fitton J. G. (2007) The OIB Paradox. In *Plates, Plumes, and Planetary Processes, Geological Society of America Special Paper 430* pp. 387–412.

Fitton J. G. and Dunlop H. M. (1985) The Cameroon line, West Africa and its bearing on the origin of oceanic and continental alkali basalt. *Earth Planet. Sci. Lett.* **72**, 23–38.

Gale A., Dalton C. A., Langmuir C. H., Su Y. and Schilling J.-G. (2013) The mean composition of ocean ridge basalts. *Geochem Geophys Geosy* **14**, 489–518.

Gall L. (2011) Development and Application of Nickel Stable Isotopes as a New Geochemical Tracer. University of Oxford.

Gall L., Williams H. M., Halliday A. N. and Kerr A. C. (2017) Nickel isotopic composition of the mantle. *Geochim. Cosmochim. Acta* **199**, 196–209.

Gall L., Williams H., Siebert C. and Halliday A. (2012) Determination of mass-dependent variations in nickel isotope compositions using double spiking and MC-ICPMS. *J. Anal. At. Spectrom.* **27**, 137–145.

Gramlich J. W., Machlan L. A., Barnes I. L. and Paulsen P. J. (1989) Absolute isotopic abundance ratios and atomic weight of a reference sample of nickel. *J. Res. Natl. Inst. Stand. Technol.* **94**, 347.

Green D. H. (1970) A review of experimental evidence on the origin of basaltic and nephelinitic magmas. *Phys. Earth Planet. Inter*. **3**, 221–235.

Gueguen B., Rouxel O., Ponzevera E., Bekker A. and Fouquet Y. (2013) Nickel isotope variations in terrestrial silicate rocks and geological reference materials measured by MC-ICP-MS. *Geostand. Geoanalytical Res.* **37**, 297–317.

Guignard J., Quitté G., Méheut M., Toplis M. J., Poitrasson F., Connetable D. and Roskosz M. (2020) Nickel isotope fractionation during metal-silicate differentiation of planetesimals: Experimental petrology and ab initio calculations. *Geochim. Cosmochim. Acta* **269**, 238–256.

Guimarães A. R., Fitton J. G., Kirstein L. A. and Barfod D. N. (2020) Contemporaneous intraplate magmatism on conjugate South Atlantic margins: A hotspot conundrum. *Earth Planet. Sci. Lett.* **536**, 116147.

Haase K. M., Regelous M., Duncan R. A., Brandl P. A., Stroncik N. and Grevemeyer I. (2011) Insights into mantle composition and mantle melting beneath mid-ocean ridges from postspreading volcanism on the fossil Galapagos Rise. *Geochem Geophys Geosy* **12**, 1–21.

Halliday A. N., Davidson J. P., Holden P., DeWolf C., Lee D.-C. and Fitton J. G. (1990) Trace-element fractionation in plumes and the origin of HIMU mantle beneath the Cameroon line. *Nature* **346**, 818–822.

Halliday A. N., Davies G. R., Lee D.-C., Tommasini S., Paslick C. R., Fitton J. G. and James D. E. (1992) Lead isotope evidence for young trace element enrichment in the oceanic upper mantle. *Nature* **359**, 623–627.

Halliday A. N., Lee D.-C., Tommasini S., Davies G. R., Paslick C. R., Fitton J. G., and James D. E. (1995) Incompatible trace elements in OIB and MORB and source enrichment in the sub-oceanic mantle. *Earth Planet. Sci. Lett.* **133**, 379–395.

Hardarson B. S. and Fitton J. G. (1997) Mechanisms of crustal accretion in Iceland. *Geology* **25**, 1043–1046.

Harpp K. S. and White W. M. (2001) Tracing a mantle plume: Isotopic and trace element variations of Galápagos seamounts. *Geochem Geophys Geosy* **2**(6), 1525-2027

Hauri E. H. (1996) Major-element variability in the Hawaiian mantle plume. *Nature* **386**.

Hawkesworth C. J., Norry M. J., Roddick J. C. and Vollmer R. (1979) 143Nd/144Nd and 87Sr/86Sr ratios from the Azores and their significance in LIL-element enriched mantle. *Nature* **280**, 28–31.

Hofmann A., Bekker A., Dirks P., Gueguen B., Rumble D. and Rouxel O. J. (2014) Comparing orthomagmatic and hydrothermal mineralization models for komatiite-hosted nickel deposits in Zimbabwe using multiple-sulfur, iron, and nickel isotope data. *Miner. Depos.* **49**, 75–100.

Hofmann A. W. (1997) Mantle geochemistry: the message from oceanic volcanism. *Nature* **385**, 219–229.

Hofmann A. W. and White W. M. (1982) Mantle plumes from ancient oceanic crust. *Earth Planet. Sci. Lett.* **57**, 421–436.

Jackson M. G., Konter J. G. and Becker T. W. (2017) Primordial helium entrained by the hottest mantle plumes. *Nature* **542**, 340–343.

Kempton P. D., Fitton J. G., Saunders A. D., Nowell G. M., Taylor R. N., Hardarson B. S. and Pearson G. (2000) The Iceland plume in space and time: a Sr-Nd-Pb-Hf study of the North Atlantic rifted margin. *Earth Planet. Sci. Lett.* **177**, 255–271.

Klaver M., Ionov D. A., Takazawa E. and Elliott T. (2020) The non-chondritic Ni isotope composition of Earth's mantle. *Geochim. Cosmochim. Acta* **268**, 405–421.

Klein E. and Langmuir C. H. (1987) Global correlations of ocean ridge basalt chemistry with axial depth and crustal thickness. *J. Geophys. Res.* **92**, 8089–8115.

739 Kristjansson L., Gudmundsson A. and Hardarson B. S. (2004) Stratigraphy and paleomagnetism of a 2.9-km
740 composite lava section in Eyjafjördur, Northern Iceland: a reconnaissance study. *Int J Earth Sci* **93**,
741 582–595.

742 Le Roex A. P., Bell D. R. and Davis P. (2003) Petrogenesis of group I Kimberlites from Kimberley, South
743 Africa: Evidence from bulk-rock geochemistry. *J. Petrol.* **44**, 2261–2286.

744 Lee D.-C., Halliday A. N., Fitton J. G. and Poli G. (1994) Isotopic variations with distance and time in the
745 volcanic islands of the Cameroon line: evidence for a mantle plume origin. *Earth Planet. Sci. Lett.* **123**,
746 119–138.

747 Lesher C. E., Dannberg J., Barfod G. H., Bennett N. R., Glessner J. J. G., Lacks D. J. and Brenan J. M.
748 (2020) Iron isotope fractionation at the core–mantle boundary by thermodiffusion. *Nat. Geosci.* **13**,
749 382–386.

750 Li M., Grasby S. E., Wang S. J., Zhang X., Wasylenki L. E., Xu Y., Sun M., Beauchamp B., Hu D. and Shen
751 Y. (2021) Nickel isotopes link Siberian Traps aerosol particles to the end-Permian mass extinction.
752 *Nat. Commun.* **12**, 1–7.

753 Liu J., Dauphas N., Roskosz M., Hu M. Y., Yang H., Bi W., Zhao J., Alp E. E., Hu J. Y. and Lin J. F. (2017)
754 Iron isotopic fractionation between silicate mantle and metallic core at high pressure. *Nat. Commun.* **8**,
755 1–6.

756 McDonough W. F. and Sun S. -s. (1995) The composition of the Earth. *Chem. Geol.* **120**, 223–253.

757 Moreira M., Doucelance R., Kurz M. D., Dupré B. and Allègre C. J. (1999) Helium and lead isotope
758 geochemistry of the Azores archipelago. *Earth Planet. Sci. Lett.* **169**, 189–205.

759 Murton B. J. and Rona P. A. (2015) Carlsberg Ridge and Mid-Atlantic Ridge: Comparison of slow spreading
760 centre analogues. *Deep. Res. Part II Top. Stud. Oceanogr*. **121**, 71–84.

761 Nicholls D. (1974) Complexes and first row transition elements., Macmillan, London.

762 Niu Y. and Batiza R. (1997) Trace element evidence from seamounts for recycled oceanic crust in the
763 Eastern Pacific mantle. *Earth Planet. Sci. Lett.* **148**, 471–483.

764 Niu Y. and O'Hara M. J. (2009) MORB mantle hosts the missing Eu (Sr, Nb, Ta and Ti) in the continental
765 crust: New perspectives on crustal growth, crust-mantle differentiation and chemical structure of
766 oceanic upper mantle. *Lithos* **112**, 1–17.

767 Pašava J., Chrastný V., Loukola-Ruskeeniemi K. and Šebek O. (2019) Nickel isotopic variation in black
768 shales from Bohemia, China, Canada, and Finland: a reconnaissance study. *Miner. Depos.* **54**, 719–
769 742.

770 Paslick C. R. (1995) A Geochemical study of volcanism associated with the early stages of continental
771 rifting in Northern Tanzania. University of Michigan.

772 Paulick H., Bach W., Godard M., De Hoog J. C. M., Suhr G. and Harvey J. (2006) Geochemistry of abyssal
773 peridotites (Mid-Atlantic Ridge, 15°20′N, ODP Leg 209): Implications for fluid/rock interaction in
774 slow spreading environments. *Chem. Geol*. **234**, 179–210.

775 Pearson D. G. and Nowell G. M. (2004) Re-Os and Lu-Hf Isotope Constraints on the Origin and Age of
776 Pyroxenites from the Beni Bousera Peridotite Massif: Implications for Mixed Peridotite-Pyroxenite
777 Mantle Sources. *J. Petrol.* **45**, 439–455.

778 Ratié G., Jouvin D., Garnier J., Rouxel O., Miska S., Guimarães E., Cruz Vieira L., Sivry Y., Zelano I.,
779 Montarges-Pelletier E., Thil F. and Quantin C. (2015) Nickel isotope fractionation during tropical
780 weathering of ultramafic rocks. *Chem. Geol.* **402**, 68–76.

781 Ratié G., Quantin C., Jouvin D., Calmels D., Ettler V., Sivry Y., Vieira L. C., Ponzevera E. and Garnier J.

(2016) Nickel isotope fractionation during laterite Ni ore smelting and refining: Implications for tracing the sources of Ni in smelter-affected soils. *Appl. Geochemistry* **64**, 136–145.

Ratié G., Quantin C., Maia De Freitas A., Echevarria G., Ponzevera E. and Garnier J. (2019) The behavior of nickel isotopes at the biogeochemical interface between ultramafic soils and Ni accumulator species. *J. Geochemical Explor.* **196**, 182–191.

Rizo H., Andrault D., Bennett N. R., Humayun M., Brandon A., Vlastelic I., Moine B., Poirier A., Bouhifd M. A. and Murphy D. T. (2019) $^{182}$W evidence for core-mantle interaction in the source of mantle plumes. *Geochem. Persp. Let* **11**, 6–11.

Saunders N. J., Barling J., Harvey J. and Halliday A. N. (2020) Heterogeneous nickel isotope compositions in the terrestrial mantle – Part 1: Ultramafic lithologies. *Geochim. Cosmochim. Acta* **285**, 129–149.

Schaefer B. F., Turner S., Parkinson I., Rogers N. and Hawkesworth C. (2002) Evidence for recycled Archaean oceanic mantle lithosphere in the Azores plume. *Nature* **420**, 304–307.

Shannon R. D. (1976) Revised Effective Ionic Radii and Systematic Studies of Interatomie Distances in Halides and Chaleogenides., *Acta Cryst.***32**, 751-767

Siebert C., Nägler T. F. and Kramers J. D. (2001) Determination of molybdenum isotope fractionation by double-spike multicollector inductively coupled plasma mass spectrometry. *Geochem Geophys Geosy* **2**, 1032.

Sossi P. A., Foden J. D. and Halverson G. P. (2012) Redox-controlled iron isotope fractionation during magmatic differentiation: An example from the Red Hill intrusion, S. Tasmania. *Contrib. Mineral. Petrol.* **164**, 757–772.

Spivak-Birndorf L. J., Wang S.-J., Bish D. L. and Wasylenki L. E. (2018) Nickel isotope fractionation during continental weathering. *Chem. Geol.* **476**, 316–326.

Steele R. C. J., Elliott T., Coath C. D. and Regelous M. (2011) Confirmation of mass-independent Ni isotopic variability in iron meteorites. *Geochim. Cosmochim. Acta* **75**, 24, 7906–7925.

Suh C. E., Luhr J. F. and Njome M. S. (2008) Olivine-hosted glass inclusions from Scoriae erupted in 1954-2000 at Mount Cameroon volcano, West Africa. *J. Volcanol. Geotherm. Res.* **169**, 1–33.

Teng F. Z., Dauphas N., Huang S. and Marty B. (2013) Iron isotopic systematics of oceanic basalts. *Geochim. Cosmochim. Acta* **107**, 12–26.

Volpe A. M., Douglas Macdougall J. and Hawkins J. W. (1987) Mariana Trough basalts (MTB): trace element and SrNd isotopic evidence for mixing between MORB-like and Arc-like melts. *Earth Planet. Sci. Lett.* **82**, 241–254.

Wang S. J., Rudnick R. L., Gaschnig R. M., Wang H. and Wasylenki L. E. (2019) Methanogenesis sustained by sulfide weathering during the Great Oxidation Event. *Nat. Geosci.* **12**, 296–300.

Wang S. J., Wang W., Zhu J. M., Wu Z., Liu J., Han G., Teng F. Z., Huang S., Wu H., Wang Y., Wu G. and Li W. (2021) Nickel isotopic evidence for late-stage accretion of Mercury-like differentiated planetary embryos. *Nat. Commun.* **12**, 1–7.

Watkins N. D. and Walker G. P. L. (1977) Magnetostratigraphy of Eastern Iceland. *Am J Sci* **277**, 513–584.

Weyer S., Mezger K., Woodland A. B., Brey G. P., Anbar A. D. and Münker C. (2007) Fe-isotope fractionation during partial melting on Earth and the current view on the Fe-isotope budgets of the planets (reply to the comment of F. Poitrasson and to the comment of B.L. Beard and C.M. Johnson on "Iron isotope fractionation during planetary. *Earth Planet. Sci. Lett.* **256**, 638–646.

White W. M., McBirney A. R. and Duncan R. A. (1993) Petrology and geochemistry of the Galápagos Islands: Portrait of a pathological mantle plume. *J. Geophys. Res.* **98**, 533–563.

White W. M., Tapia M. D. M. and Schilling J.-G. (1979) The Petrology and Geochemistry of the Azores Islands. *Contrib. Mineral. Petrol.* **69**, 201–213.

Widom E. and Shirey S. B. (1996) Os isotope systematics in the Azores: Implications for mantle plume sources. *Earth Planet. Sci. Lett.* **142**, 451–465.

Williams H. M., McCammon C. A., Peslier A. H., Halliday A. N., Teutsch N., Levasseur S. and Burg J.-P. (2004) Iron Isotope Fractionation and the Oxygen Fugacity of the Mantle. *Science* **304**, 1656–1659.

Williams H. M., Nielsen S. G., Renac C., Griffin W. L., O'Reilly S. Y., McCammon C. A., Pearson N., Viljoen F., Alt J. C., Halliday A. N. (2009) Fractionation of oxygen and iron isotopes by partial melting processes: Implications for the interpretation of stable isotope signatures in mafic rocks. *Earth Planet. Sci. Lett.* **283**, 156–166.

Williams H. M., Peslier A. H., McCammon C. and Halliday A. N. (2005) Systematic iron isotope variations in mantle rocks and minerals: The effects of partial melting and oxygen fugacity. *Earth Planet. Sci. Lett.* **235**, 435–452.

Wood B. J., Smythe J. and Harrison T. (2019) The condensation temperatures of the elements: A reappraisal. *Am. Mineral.* **104**, 844–856.

Workman R. K. and Hart S. R. (2005) Major and trace element composition of the depleted MORB mantle (DMM). *Earth Planet. Sci. Lett.* **231**, 53–72.

Xu Y. (2002) Evidence for crustal components in the mantle and constraints on crustal recycling mechanisms: pyroxenite xenoliths from Hannuoba, North China. *Chem. Geol.* **182**, 301–322.

Yi W., Halliday A. N., Alt J. C., Lee D.-C., Rehkamper M., Garcia M. O., Langmuir C. H. and Su Y. (2000) Cadmium, indium, tin, tellurium, and sulfur in oceanic basalts: Implications for chalcophile element fractionation in the Earth. *J. Geophys. Res.* **105**, 18927–18949.

Yi W., Halliday A. N., Lee D.-C. and Christensen J. N. (1995) Indium and tin in basalts, sulfides, and the mantle. *Geochim. Cosmochim. Acta* **59**, 5081–5090.

Zhang C., Zhang L., Bader T., Song S. and Lou Y. (2013) Geochemistry and trace element behaviors of eclogite during its exhumation in the Xitieshan terrane, North Qaidam UHP belt, NW China. *J. Asian Earth Sci.* **63**, 81–97.

Zindler A. and Hart S. (1986) Chemical Geodynamics. *Annu. Rev. Earth Planet. Sci.* **14**, 493–571.

# Electronic Appendices

## Tables

### Table EA1

| Sample Code | Lithology | Locality | $SiO_2$ | $Al_2O_3$ | $Fe_2O_3$ | MgO | CaO | $Na_2O$ | $K_2O$ | $TiO_2$ | $P_2O_5$ |
|---|---|---|---|---|---|---|---|---|---|---|---|
| R82-1 [B] | N type MORB | East Pacific Ridge | 49.3 | 16.07 | 8.67 | 9.17 | 12.77 | 2.32 | 0.06 | 1.06 | 0.13 |
| R94-2 [B] | N type MORB | East Pacific Ridge | 51 | 14.52 | 10.2 | 7.59 | 12.05 | 2.55 | 0.1 | 1.33 | 0.14 |
| R93-7 [B] | E type MORB | East Pacific Ridge | 49.48 | 16.84 | 8.29 | 8.63 | 11.77 | 2.77 | 0.21 | 1.36 | 0.19 |
| A127 D5-5 [A] | N type MORB | Mid Atlantic Ridge | 49.57 | 16.39 | 2.22 | 9.37 | 12.92 | 2 | 0.05 | 0.79 | 0.06 |
| A127 D8-2 [A] | N type MORB | Mid Atlantic Ridge | 50.08 | 16.25 | 2.49 | 9.43 | 12.31 | 2.24 | 0.04 | 0.81 | 0.07 |
| A127 D10-2A | MORB | Mid Atlantic Ridge | NA | NA | NA | NA | NA | NA | NA | NA | NA |
| A127 D15-1 [A] | E type MORB | Mid Atlantic Ridge | 51.44 | 14.74 | 2.44 | 8.08 | 12.03 | 2.2 | 0.19 | 1.05 | 0.14 |
| A127 D17-3 [A] | E type MORB | Mid Atlantic Ridge | 49.14 | 16.06 | 2.52 | 8.39 | 13.71 | 2.27 | 0.67 | 1.35 | 0.25 |
| A127 D21-3 [A] | E type MORB | Mid Atlantic Ridge | 50.98 | 15.74 | 3.73 | 5.84 | 10.64 | 3.36 | 1.09 | 2.17 | 0.4 |
| A127 D22-5 [A] | E type MORB | Mid Atlantic Ridge | 51.86 | 15.09 | 3.09 | 6.03 | 10.62 | 2.78 | 0.94 | 1.97 | 0.34 |
| A127 D26-5 [A] | E type MORB | Mid Atlantic Ridge | 51.38 | 14.51 | 2.59 | 7.57 | 11.14 | 2.33 | 0.18 | 1.34 | 0.15 |
| A127 D27-5 [A] | E type MORB | Mid Atlantic Ridge | 51.49 | 15.29 | 2.53 | 7.99 | 11.97 | 2.28 | 0.3 | 1.21 | 0.16 |
| AZF3 | transitional basalt | Flores, Azores | NA | NA | NA | 10.6 | NA | NA | 0.69 [C] | 1.83 | 0.39 [C] |
| AZFY2 [C] | alkali basalt | Fayal, Azores | NA | NA | NA | 10.18 | NA | NA | 0.99 [C] | 2.67 | 0.40 [C] |
| AZP6 [C] | alkali basalt | Pico, Azores | NA | NA | NA | 6.19 | NA | NA | 1.35 [C] | 3.66 | 0.78 [C] |
| PL02 25-1 [A] | alkali basalt | Galápagos | 46.71 | 15.31 | 4.49 | 5.15 | 9.64 | 4.04 | 1.2 | 3.72 | NA |
| PL02 30-1 [A] | tholeiite | Galápagos | 48.67 | 16.58 | 2.88 | 8.32 | 12.25 | 2.59 | 0.36 | 1.56 | 0.17 |
| D4-6G [A] | alkali basalt | Lōʻihi, | 46.8 | 15.8 | 11.06 | 6 | 10.6 | 3 | 0.56 | 3.24 | 0.38 |
| T38 [F] | tholeiite | N, Iceland | 47.61 | 14.35 | 12.78 | 7.57 | 11.16 | 2.22 | 0.45 | 2.16 | 0.26 |
| GS18 [F] | tholeiite | N, Iceland | 46.95 | 17.66 | 10.6 | 6.37 | 13.01 | 1.72 | 0.24 | 1.42 | 0.15 |
| CX11 [F] | tholeiite | E, Iceland | 46.72 | 13.83 | 14.86 | 5.59 | 9.59 | 2.71 | 0.63 | 3.44 | 0.44 |
| CX19 [F] | tholeiite | E, Iceland | 48.69 | 15.4 | 12.26 | 6.39 | 12.02 | 2.23 | 0.3 | 2.12 | 0.21 |
| SNB19 [F, H] | tholeiite | W, Iceland | 45.63 | 14.53 | 11.93 | 11.48 | 11.84 | 2 | 0.69 | 2.27 | 0.45 |
| SNB40 | tholeiite | W, Iceland | NA | NA | NA | 10.50 [G] | NA | NA | NA | 2.63 | NA |
| SNB42 [F, H] | tholeiite | W, Iceland | 45.20 | 14.77 | 11.67 | 10.64 | 11.64 | 2.14 | 0.62 | 2.28 | 0.47 |

| | | | | | | | | | | | | |
|---|---|---|---|---|---|---|---|---|---|---|---|---|
| P18 | olivine nephelinite | Príncipe, Island, Cameroon Line | 37.89 | 10.51 | 14.22 | 11.59 | 13.24 | 3.06 | 1.61 | 4.05 | 1.43 |
| C134 | mafic nephelinite | Etinde, Cameroon | 39.8 | 12.92 | 13.71 | 8.03 | 15.64 | 2.46 | 0.45 | 4.5 | 0.68 |
| C151 | mafic nephelinite | Etinde, Cameroon | 41.94 | 13.12 | 14.49 | 7.71 | 13.24 | 3.16 | 0.98 | 4.12 | 0.58 |
| C22 | nephelinite | Etinde, Cameroon | 40.43 | 14.56 | 12.34 | 5.26 | 13.65 | 4.32 | 2.93 | 4.04 | 1.14 |
| C20 | nephelinite | Etinde, Cameroon | 40.54 | 15.31 | 11.44 | 4.55 | 13.12 | 4.93 | 2.82 | 3.69 | 1.07 |
| C152 [D] | hauyne nephelinite | Etinde, Cameroon | 39.99 | 17.54 | 9.69 | 3.74 | 10.87 | 6.95 | 3.87 | 2.95 | 0.89 |
| C150 [C,DI] | olivine mela-nephelinite | Etinde, Cameroon | 39.6 | 12.75 | 13.91 | 8.03 | 14.98 | 2.69 | 1.66 | 4.49 | 0.67 |
| C65 [D] | Hy-normative basalt | Manengouba, Cameroon | 49.77 | 13.86 | 12.52 | 7.78 | 7.46 | 3.35 | 1.38 | 2.23 | 0.39 |
| C192 | basanite | Mt Cameroon, Cameroon | 44.7 | 15.07 | 4.09 | 6.02 | 11.86 | 3.68 | 1.31 | 3.39 | 0.56 |
| C30 | basanite | Mt Cameroon, Cameroon | 44.72 | 10.04 | 12.79 | 12.81 | 13.5 | 2.27 | 0.76 | 2.58 | 0.44 |
| C112 [D] | basanite | Bambouto, Cameroon | 43.85 | 13.65 | 12.52 | 9.21 | 10.55 | 3.47 | 1.47 | 3.1 | 1.03 |
| C51 | alkali basalt | Manengouba, Cameroon | 47.68 | 14.65 | 12.51 | 6.95 | 9.07 | 3.56 | 1.43 | 2.54 | 0.63 |
| C72 | alkali basalt | Manengouba, Cameroon | 45.72 | 14.5 | 13.16 | 7.55 | 9.01 | 3.36 | 1.74 | 3.14 | 0.67 |
| C146 | alkali basalt | Mandara Mts, Cameroon | 40.04 | 11.8 | 14.19 | 10.19 | 11.68 | 3.62 | 0.98 | 3.71 | 1.13 |
| FP44 [C,D] | alkali basalt | Bioko, Island, Cameroon Line | 44.4 | 10.8 | 13.33 | 10.8 | 12.58 | 2.48 | 1.19 | 3.51 | 0.63 |
| H93-3 [E] | foidite | Kwaraha, N Tanzania | 39.62 | 7.94 | 14.32 | 13.11 | 14.47 | 1.63 | 1.59 | 3.03 | 0.46 |
| BD105 | olivine-melilite nephelinite | Oldoinyo, Loolmurwak, Tanzania | NA | NA | NA | NA | NA | NA | NA | NA | NA |
| KH03-10L[I] | basanite | Kilbourne Hole, USA | 49.12 | 13.83 | 10.45 | 9.67 | 8.9 | 3.25 | 1.86 | 1.9 | 0.49 |
| BD780[J,K] | ankaramite | Lashaine, Tanzania | 39.44 | 5.84 | 9.21 | 17.67 | 12.24 | 1.97 | 0.99 | 2.37 | 0.81 |

NA symbolises data that is not available

All data in wt.%

**References**: [A]Yi et al., (2000); [B]Niu and Batiza, (1997); [C]Halliday et al., (1995); [D]Fitton, (1987); [E]Paslick et al., (1995); [F]Hardarson and Fitton, (1997); [G]Yi et al., (1995); [H]Kempton et al.,(2000);[I] Harvey (2012); [J]Dawson et al. (1970); [K]Ridley and Dawson (1975) in addition to determination by the authors

**Table EA2**

| Sample Code | S | Cu | Cr | V | Ba | Rb | Sr | La | Nd | Sm | Eu | Gd | Yb |
|---|---|---|---|---|---|---|---|---|---|---|---|---|---|

| | | | | | | | | | | | | | |
|---|---|---|---|---|---|---|---|---|---|---|---|---|---|
| R82-1 [B] | 1360 | 95.8 | 394 | 217 | 7.18 | 0.5 | 88.6 | 1.64 | 5.15 | 1.96 | 0.77 | 2.62 | 2.11 |
| R94-2 [B] | 1010 | 81.6 | 84 | 273 | 20.5 | 1.64 | 104 | 3.16 | 7.67 | 2.73 | 1.1 | 3.83 | 2.78 |
| R93-7 [B] | 920 | 80.3 | 298 | 207 | 25.1 | 2.01 | 177 | 6.16 | 10.74 | 3.14 | 1.15 | 3.73 | 2.5 |
| A127 D5-5 [A] | 1050 | NA | NA | NA | 8 | 0.67 | 83 | 1.24 | 3.7 | 1.5 | NA | NA | NA |
| A127 D8-2 [A] | 970 | NA | NA | NA | 6.2 | 0.68 | 87 | 1.86 | 4.72 | 1.69 | 0.69 | 2.47 | 1.97 |
| A127 D10-2A | NA | NA | NA | NA | NA | NA | NA | NA | NA | NA | NA | NA | NA |
| A127 D15-1 [A] | 725 | NA | NA | NA | 60 | 4.64 | 104 | 5.24 | 7.74 | 2.34 | 0.86 | 3.01 | 2.46 |
| A127 D17-3 [A] | 460 | NA | NA | NA | 244 | 18.8 | 295 | 16.7 | 16.2 | 3.55 | 1.19 | 4.12 | 1.94 |
| A127 D21-3 [A] | 1000 | NA | NA | NA | 258 | 23.3 | 405 | 23.7 | 25.2 | 5.49 | 1.81 | 5.94 | 2.49 |
| A127 D22-5 [A] | 1220 | NA | NA | NA | 235 | 20.5 | 282 | 20.4 | 20.7 | 4.49 | 1.51 | 5.06 | 2.43 |
| A127 D26-5 [A] | 995 | NA | NA | NA | 47 | 3.98 | 94 | 4.96 | 9.11 | 2.92 | 1.01 | 4.03 | 3.1 |
| A127 D27-5 [A] | 800 | NA | NA | NA | 82.6 | 7.53 | 134 | 7.69 | 10.4 | 2.85 | 1.0 | 3.64 | 2.44 |
| | | | | | | | | | | | | | |
| AZF3 | NA | NA | NA | NA | 422 [C] | 15.4 [C] | 641 [C] | 28.0 [C] | 26.5 [C] | 5.31 [C] | 1.94 [C] | 5.16 [C] | 2.12 [C] |
| AZFY2 | 95 | NA | NA | NA | 312 [C] | 24.9 [C] | 543 [C] | 26.3 [C] | 28.9 [C] | 6.37 [C] | 2.08 [C] | 6.3 [C] | 1.89 [C] |
| AZP6 | NA | NA | NA | NA | 359 [C] | 27 [C] | 734 [C] | 39.7 [C] | 46.1 [C] | 9.53 [C] | 3.04 [C] | NA | 2.2 [C] |
| PL02 25-1 [A] | 1160 | NA | NA | NA | 182 | 9.56 | 452 | 22.7 | 31.8 | 7.21 | 2.36 | 6.83 | 2.38 |
| PL02 30-1 [A] | 1000 | NA | NA | NA | 100 | 7.14 | 300 | 10.4 | 13.5 | 3.38 | 1.24 | 4.09 | 2.44 |
| D4-6G [A] | 2140 | NA | NA | NA | 118 | 8.37 | 440 | 15 | 23.5 | 5.97 | 2.08 | 6.44 | 2.2 |
| ST38 [E] | 32 | 99 | 268 | 325 | 199 | 7.3 | 248 | 13 | 19 | NA | NA | NA | NA |
| GS18 [E] | 20 | 106 | 212 | 270 | 33 | 3.4 | 200 | 6 | 12 | NA | NA | NA | NA |
| CX11 [E] | NA | 70 | 109 | 344 | 167 | 11.4 | 312 | 17 | 33 | NA | NA | NA | NA |
| CX19 [E] | 40 | 116 | 265 | 310 | 61 | 5.5 | 268 | 9 | 20 | NA | NA | NA | NA |
| SNB19 [F] | 37 | 81 | 635 | 317 | 383 | 13.1 | 449 | 24.7 | 28.3 | 5.72 | 1.97 | 5.31 | 1.91 |
| SNB40 | 86 | NA | NA | NA | 359 [G] | 14.0 [G] | 449 | 23.4 | NA | 5.7 [G] | NA | NA | NA |
| SNB42 [F] | NA | 77 | 652 | 325 | 299 | 11 | 426 | 21 | 23 | NA | NA | NA | NA |
| | | | | | | | | | | | | | |
| P18 | NA | 55.9 | 338 | 307 | 987 | 39.7 | 1297 | 103 | 82.5 | 14.9 | NA | NA | NA |
| C134 | NA | 114 | 111 | 441 | 752 | 75.5 | 1574 | 100 | NA | NA | NA | NA | NA |
| C151 | NA | 115.6 | 161 | 374 | 508 | 52.5 | 1020 | 77.7 | NA | NA | NA | NA | NA |
| C22 | NA | 61.9 | 9.3 | 447 | 942 | 89.2 | 2204 | 235 | NA | NA | NA | NA | 3.8 [H] |
| C20 | NA | 61.5 | 12.8 | 391 | 1423 | 85.2 | 3272 | 247 | NA | NA | NA | NA | 4.3 [H] |
| C152 | NA | 83.6 | 5.4 | 342 | 1006 | 114 | 2395 | 225 | 142 | NA | NA | NA | 3.6 [H] |
| C150 | NA | 112.6 | 126 | 456 | 788 | 89.1 | 1054 | 97 | 89.6 | 14.3 | NA | NA | 1.7 [H] |
| C65 | NA | 56.6 | 275 | 193 | 458 | 30.7 | 429 | 41.3 | 33.2 | NA | NA | NA | NA |
| C192 | NA | 101 | 55 | 347 | 410 | 29 | 871 | 61 | 54 | NA | NA | NA | 2.1 [H] |
| C30 | NA | 95.5 | 872 | 299 | 292 | 22.2 | 625 | 45.1 | 44.4 | NA | NA | NA | 1.7 [H] |
| C112 | 291 | 43 | 459 | 232 | 874 | 31.7 | 1242 | 42.9 | 45.8 | NA | NA | NA | NA |
| C51 | NA | 54.9 | 220 | 188 | 439 | 36.8 | 757 | 46.1 | 46.3 | NA | NA | NA | 1.8 [H] |
| C72 | NA | 44.2 | 150 | 239 | 526 | 42.7 | 918 | 60.4 | 53.8 | NA | NA | NA | 1.9 [H] |
| C146 | 368 | 47.8 | 274 | 535 | 609 | 24.5 | 1157 | 62.1 | 52.9 | NA | NA | NA | NA |
| FP44 | 136 | 71.6 | 521 | 294 | 562 [C] | 32.5 [C] | 823 [C] | 58.3 [C] | 48.7 [C] | 9.72 [C] | NA | NA | NA |
| H93-3 [D] | NA | 192 | 654 | 276 | 910 | 70 | 1061 | 47 | 39 | NA | NA | NA | NA |
| BD105 | NA | NA | NA | NA | NA | NA | NA | NA | NA | NA | NA | NA | NA |
| KH03-10L [I] | NA | NA | NA | NA | 578 | 33.6 | 655 | 35.7 | 34.27 | 6.49 | 2.05 | 6.09 | 2.55 |
| BD780 [J,K] | NA | NA | 753 | NA | 387 | 20.5 | 500 | 58 | 49.6 | 7.8 | 2.3 | 5.8 | 1 |

NA symbolises data that is not available

All data in μg $g^{-1}$

**References**: [A]Yi et al., (2000); [B]Niu and Batiza, (1997); [C]Halliday et al., (1995); [D]Paslick et al., (1995); [E]Hardarson and Fitton, (1997); [F]Kempton et al.,(2000); [G]Yi et al., (1995); [H]Liang et al., (2017); [I] Harvey (2012); [J]Dawson et al. (1970); [K]Ridley and Dawson (1975) in addition to determination by the authors

861

862 **Table EA3**

| Sample Code | $^{87}Sr/^{86}Sr$ | $^{143}Nd/^{144}Nd$ | $^{206}Pb/^{204}Pb$ |
|---|---|---|---|
| R82-1 | NA | NA | NA |
| R94-2 | NA | NA | NA |
| R93-7 | NA | NA | NA |
| A127 D5-5 | NA | NA | NA |
| A127 D8-2 | NA | NA | NA |
| A127 D10-2A | NA | NA | NA |
| A127 D15-1 | NA | NA | NA |
| A127 D17-3 [E] | 0.703212 | 0.512991 | 19.144 |
| A127 D21-3 [E] | 0.703372 | 0.512918 | 19.651 |
| A127 D22-5 [E] | 0.703369 | 0.512943 | 19.435 |
| A127 D26-5 [E] | 0.703035 | 0.513142 | 18.625 |
| A127 D27-5 [E] | 0.703113 | 0.513049 | 19.022 |
| | | | |
| AZF3 [I] | 0.70336 | 0.51295 | 19 |
| AZFY2 [I] | 0.70376 | 0.51293 | 19.06 |
| AZP6 [I] | 0.70344 | 0.512946 | 19.46 |
| PL02 25-1 [D] | 0.703319 | 0.512935 | 19.099 |
| PL02 30-1 [D] | 0.703011 | 0.512964 | 19.366 |
| D4-6G | NA | NA | NA |
| ST38 [B] | 0.703379 | 0.513036 | NA |
| GS18 [B] | 0.703154 | 0.513055 | NA |
| CX11 [B] | 0.703363 | 0.512998 | NA |
| CX19 [B] | 0.70346 | 0.513022 | NA |
| SNB19 [G] | 0.70332 | 0.513058 | NA |
| SNB40 | NA | NA | NA |
| SNB42 [G] | 0.70331 | 0.513009 | NA |
| | | | |
| P18 [A] | 0.70328 | 0.51287 | 20 |
| C134 | NA | NA | NA |
| C151 | NA | NA | NA |
| C22 | NA | NA | NA |
| C20 | NA | NA | NA |
| C152 [C] | 0.70333 | 0.512804 | 20.489 |
| C150 [C] | 0.70337 | 0.5128 | 20.29 |

| | | | |
|---|---|---|---|
| C65 [H] | 0.70313 | 0.51297 | 19.65 |
| C192 | NA | NA | NA |
| C30 | NA | NA | NA |
| C112 [H] | 0.70336 | 0.51288 | 19.61 |
| C51 [C] | 0.70308 | 0.51293 | 19.92 |
| C72 [C] | 0.70303 | 0.512867 | 20.182 |
| C146 [A] | 0.703201 | 0.51292 | 20.01 |
| FP44 [H] | 0.70327 | 0.51283 | 20.35 |
| H93-3 [F] | 0.703529 | 0.512749 | 20.937 |
| BD105 | NA | NA | NA |
| KH03-10L | NA | NA | NA |
| BD780[J] | 0.7029 | NA | NA |

NA symbolises data that is not-available

**References:** [A]ANH; [B]Hardarson and Fitton, (1997)**;** [C]Halliday et al., (1990)**;** [D]Harpp and White, (2001); [E]Dosso et al., (1999); [F]Paslick et al., (1995); [G]Kempton et al., (2000); [H]Halliday et al., (1988); [I]Halliday et al., (1992); [J]Ridley and Dawson (1975)

**Table EA4**

Model endmember compositions used in the model presented in Figures 5 and 6

| | | $\delta^{60/58}$Ni | [Ni] | K2O | Na2O | La | Sm | Eu | Gd | Rb | Sr | Yb | Nd |
|---|---|---|---|---|---|---|---|---|---|---|---|---|---|
| | | ‰ | μg g$^{-1}$ | wt.% | wt.% | μg g$^{-1}$ | μg g$^{-1}$ | μg g$^{-1}$ | μg g$^{-1}$ | μg g$^{-1}$ | μg g$^{-1}$ | μg g$^{-1}$ | μg g$^{-1}$ |
| model1 | Endmember 1, preferred | -0.075 | 1450 | 0.008 | 0.020 | 0.400 | 0.200 | 2.50 | 0.020 | 0.450 | 0.085 | 0.055 | 0.320 |
| | Endmember 2, DMM [A] | +0.23 | 1886 | 0.006 | 0.130 | 0.192 | 0.050 | 7.66 | 0.365 | 0.581 | 0.239 | 0.100 | 0.358 |
| model2 | Endmember 1, average pyroxenite [B,C] | -0.075 | 794.0 | 0.100 | 0.500 | 3.60 | 1.50 | 70 | 0.940 | 5.70 | 1.40 | 0.500 | 1.54 |
| | Endmember 2, DMM [A] | +0.23 | 1886 | 0.006 | 0.130 | 0.192 | 0.050 | 7.66 | 0.365 | 0.581 | 0.239 | 0.100 | 0.358 |
| model3 | Endmember 1, kimberlite [D] | -0.075 | 1126 | 1.06 | 0.190 | 153.3 | 60.0 | 1266 | 0.860 | 131.3 | 18.9 | 4.81 | 11.4 |
| | Endmember 2, DMM [A] | +0.23 | 1886 | 0.006 | 0.130 | 0.192 | 0.050 | 7.66 | 0.365 | 0.581 | 0.239 | 0.100 | 0.358 |
| model4 | Endmember 1, kimberlite [D] | -0.075 | 1126 | 1.06 | 0.190 | 153.3 | 60.0 | 1266 | 0.860 | 131.3 | 18.9 | 4.81 | 11.4 |
| | Endmember 2, DMORB [E] | +0.23 | 100.0 | 0.10 | 2.71 | 3.12 | 1.05 | 111.0 | 3.31 | 9.46 | 3.32 | 1.30 | 4.43 |

[A] Workman and Hart (2005),
[B] Xu (2002),
[C] Saunders et al. (2020),
[D] Le Roex e al. (2003),
[E] Gale et al. (2013).

870 **EA.5 Comparison between sample processing methods**

871 Before discussing whole rock $\delta^{60/58}$Ni analysed in this work, it is necessary to test the validity of results from
872 archive powders, relative to those from fresh sample preparations. The nephelinite samples from Etinde
873 volcano in Cameroon had extremely low Ni concentrations, which were likely to make any perturbation in
874 Ni isotopic composition by the processing method or storage significant and easily observable in the results.
875 Therefore, one objective of the Cameroon Line study was to test for any difference in the $\delta^{60/58}$Ni, or Ni
876 concentration, between the original rock powders and duplicates prepared from original hand specimens to
877 current geochemistry standards.

878 Results are presented in Table EA5. All but one sample had $\delta^{60/58}$Ni within analytical uncertainty in both
879 preparations, with external reproducibility of ±0.06 ‰. The Ni concentration (calculated from isotope
880 dilution) was always fractionally greater in the new preparation, suggesting that no Ni was added during the
881 original sample preparation. This provides evidence that it is highly unlikely that any perturbation of the Ni
882 was introduced through old preparation methods, and that use of archive powders for investigation of $\delta^{60/58}$Ni
883 is effective.

884 **Table EA5**

885 Comparison between Ni isotopic composition analysed in this study for nephelinites from Etinde, Cameroon prepared
886 from archive powders or fresh preparation

| | | ORIGINAL POWDER | | | | NEW PREPARATION | | | |
|---|---|---|---|---|---|---|---|---|---|
| **Sample Code** | **Lithology** | **Ni (µg g$^{-1}$)** | **$\delta^{60/58}$Ni** | **2sd** | **n** | **Ni (µg g$^{-1}$)** | **$\delta^{60/58}$Ni** | **2sd** | **n** |
| C20 | Nephelinite | 11.8 | **+0.080** | | 1 | 12.6 | **+0.066** | 0.047 | 3 |
| C22 | Nephelinite | 9.95 | **+0.077** | 0.030 | 3 | 13.17 | **+0.073** | 0.040 | 3 |
| C150 | Olivine melanephelinite | 41.7 | **+0.038** | 0.069 | 3 | 44.4 | **+0.100** | 0.019 | 3 |
| C151 | Mafic nephelinite | 91.8 | **+0.054** | 0.030 | 3 | 92.5 | **+0.078** | 0.006 | 2 |
| C152 | Hauyne nephelinite | 7.2 | **+0.145** | 0.048 | 2 | 8.37 | **+0.078** | 0.008 | 3 |

Nickel concentrations from isotope dilution. n is the number of separate analyses of the sample (>3 means the sample was analysed more than once from separate chemistries). External reproducibility for Ni isotopic composition is ±0.06 ‰.

887

888 **Figures**

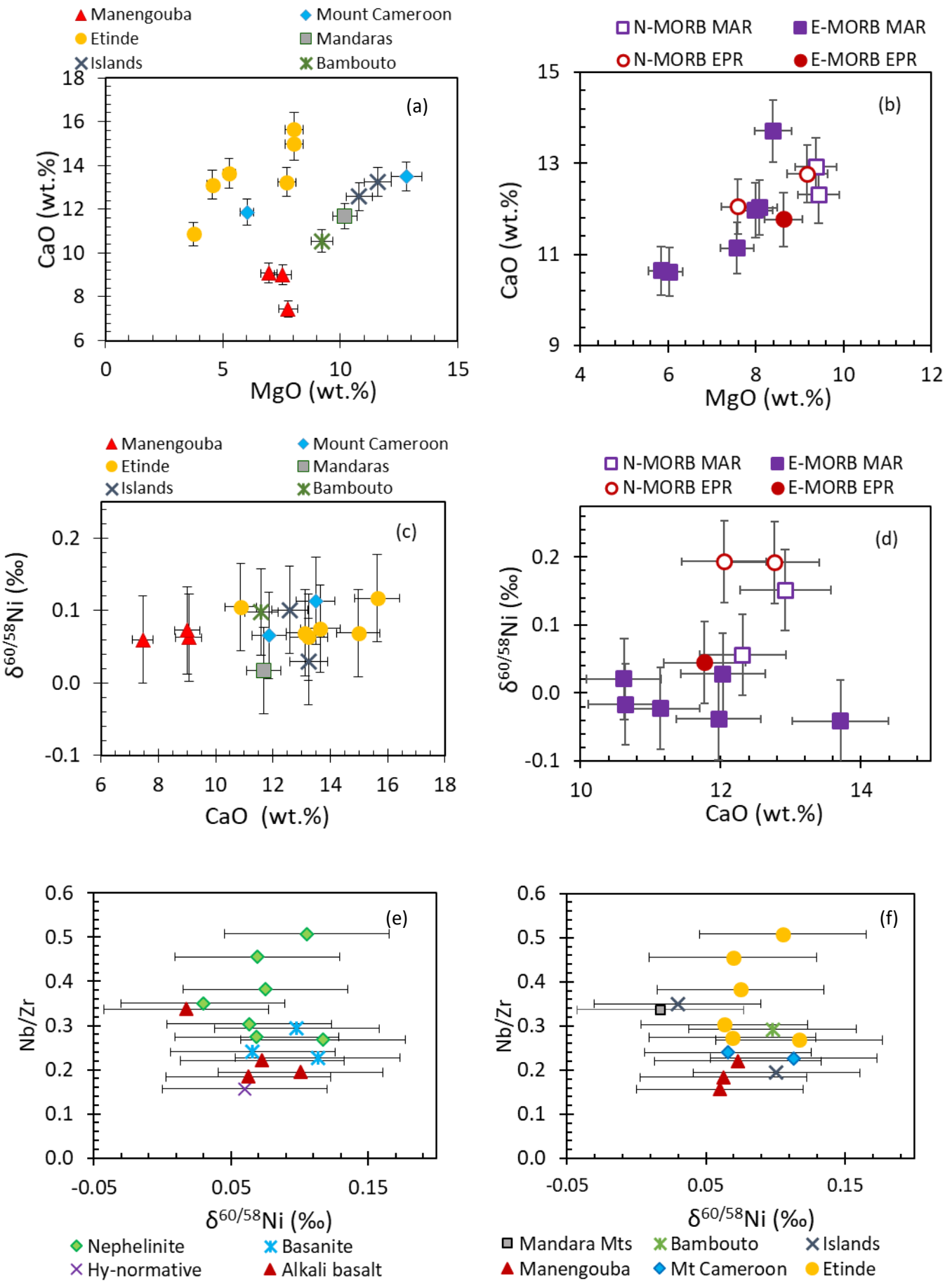
Manengouba
Mount Cameroon
Etinde
Mandaras
Islands
Bambouto
(a)
CaO (wt.%)
MgO (wt.%)
N-MORB MAR
E-MORB MAR
N-MORB EPR
E-MORB EPR
(b)
CaO (wt.%)
MgO (wt.%)
Manengouba
Mount Cameroon
Etinde
Mandaras
Islands
Bambouto
(c)
δ60/58Ni (‰)
CaO (wt.%)
N-MORB MAR
E-MORB MAR
N-MORB EPR
E-MORB EPR
(d)
δ60/58Ni (‰)
CaO (wt.%)
(e)
Nb/Zr
δ60/58Ni (‰)
Nephelinite
Basanite
Hy-normative
Alkali basalt
(f)
Nb/Zr
δ60/58Ni (‰)
Mandara Mts
Bambouto
Islands
Manengouba
Mt Cameroon
Etinde

889

890 **Figure EA1**

891 Relationship within the Cameroon Line samples (a, c, e, f) and MORB samples (b, d) with geochemical parameters used to show
892 melting and crystal fractionation within volcanic suites. Despite linear trends observed in (a) and (b) associated with melting
893 relationships, the same parameter with Ni isotopic composition shows no relationship. Error bars provided at ±0.06 ‰ for Ni
894 isotopic composition and ±5% for all other parameters.

895

896

897

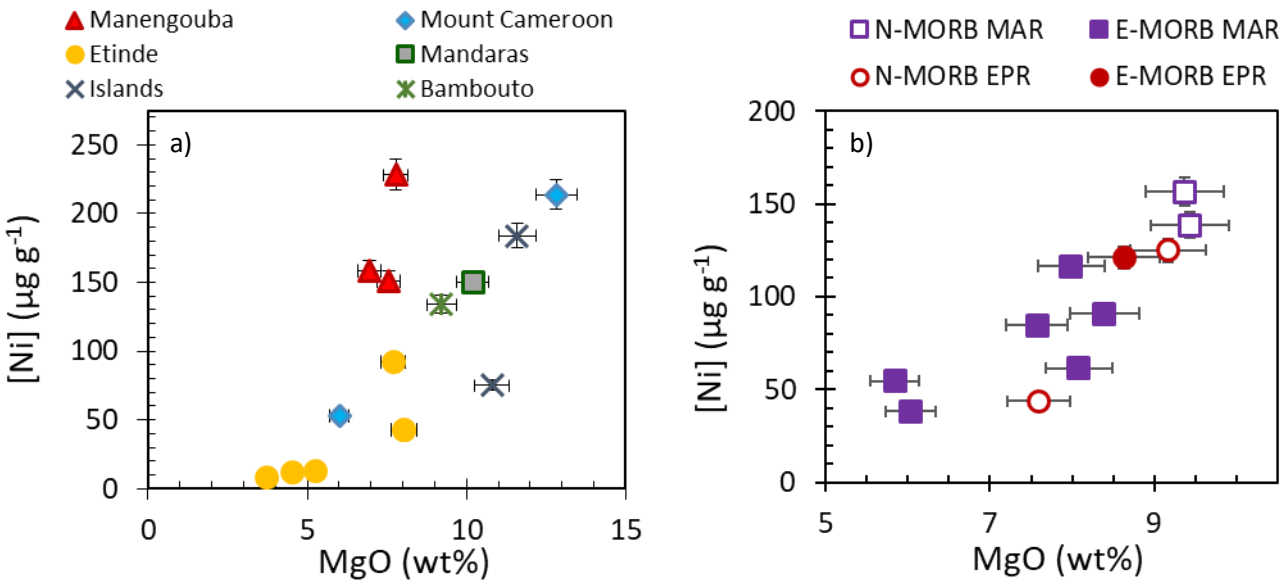


898
899 **Figure EA2**

900 Relationship between MgO and Ni concentration for (a) the Cameroon Line and (b) MORB. Data for MgO from (a) Fitton (2007) and
901 (b) Yi et al. (2000) and Niu and Batiza (1997). Ni concentration is measured by isotope dilution by MC-ICPMS. Error bars provided at
902 ±5%.

903

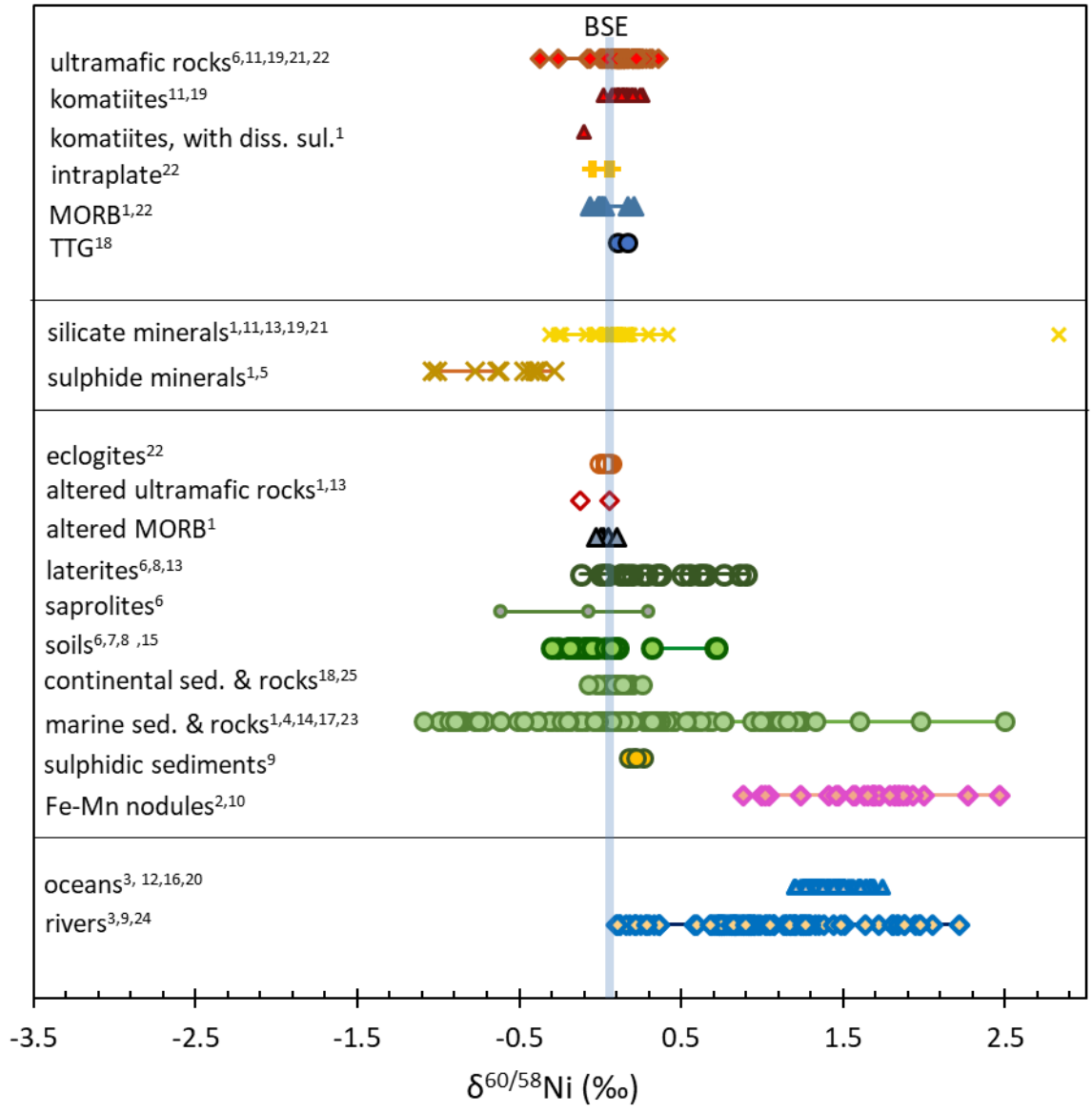


**Figure EA3**

Published Ni isotope data for terrestrial samples, excluding reference materials.

1(Gueguen et al., 2013); 2(Gall et al., 2013); 3(Cameron and Vance, 2014); 4(Porter et al., 2014); 5(Hofmann et al., 2014); 6(Ratié et al., 2015); 7(Estrade et al., 2015); 8(Ratié et al., 2016); 9(Vance et al., 2016); 10(Gueguen et al., 2016); 11(Gall et al., 2017); 12(Takano et al., 2017); 13(Spivak-Birndorf et al., 2018); 14(Ciscato et al., 2018); 15(Ratié et al., 2019); 16(R.-M. Wang et al., 2019); 17(Pašava et al., 2019); 18(S.-J. Wang et al., 2019); 19(Klaver et al., 2020); 20(Archer et al., 2020); 21(Saunders et al., 2020); 22(Wang et al., 2021); 23(Gueguen and Rouxel, 2021); 24(Revels et al., 2021); 25(Li et al., 2021)

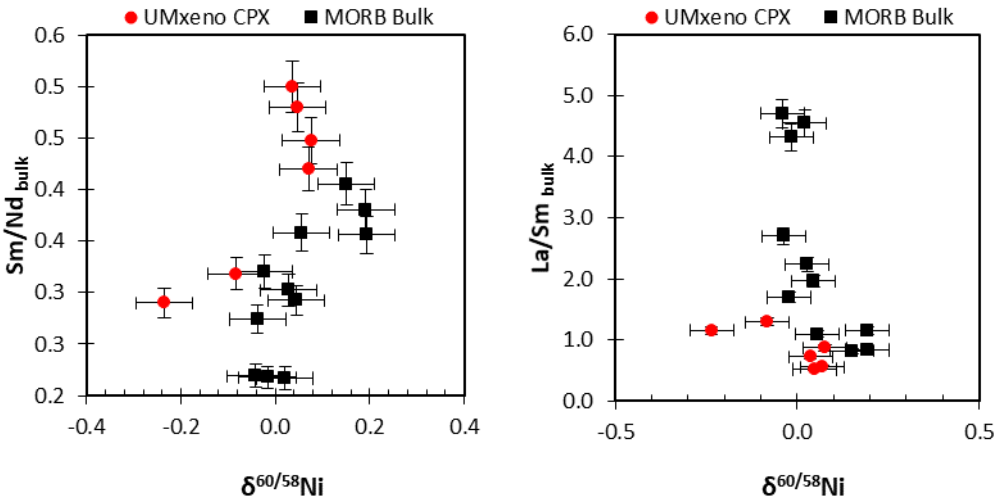


912

913 **Figure EA4**

914 Nickel isotope data of MORB samples (black squares) and of clinopyroxene separates from ultramafic xenoliths (red circles, from
915 Saunders et al., 2020). Clinopyroxene Ni isotope composition is comparably correlated with bulk xenolith Sm/Nd, (linear regression
916 $R^2 = 0.75$) and bulk rock La/Sm (linear regression $R^2 = 0.58$). Trace xenolith element data from Harvey et al.(2012); and Lee (1994)
917 also presented in Saunders et al. (2020). Error bars provided at ±0.06 ‰ for Ni isotopic composition and ±5% for all other
918 parameters.

919

920

921

922 **Electronic Appendices References**

923

924 Archer C., Vance D., Milne A. and Lohan M. C. (2020) The oceanic biogeochemistry of nickel and its
925 isotopes: New data from the South Atlantic and the Southern Ocean biogeochemical divide. *Earth*
926 *Planet. Sci. Lett*. **535**, 116118.

927 Cameron V. and Vance D. (2014) Heavy nickel isotope compositions in rivers and the oceans. *Geochim.*
928 *Cosmochim. Acta* **128**, 195–211.

929 Ciscato E. R., Bontognali T. R. R. and Vance D. (2018) Nickel and its isotopes in organic-rich sediments:
930 implications for oceanic budgets and a potential record of ancient seawater. *Earth Planet. Sci. Lett*.
931 **494**, 239–250.

932 Dawson J. B., Powell D. G. and Reid A. M. (1970) Ultrabasic Xenoliths and Lava from the Lashaine. *J. Petrol.*
933 **11**, 519–548.

934 Dosso L., Bougault H., Langmuir C., Bollinger C., Bonnier O., Etoubleau J., Dosso L., Bollinger C., Langmuir C.,
935 Bougault H. and Bonnier O. (1999) The age and distribution of mantle heterogeneity along the Mid-
936 Atlantic ridge (31-41°N). *Earth Planet. Sci. Lett*. **170**, 269–286.

Estrade, N., Cloquet, C., Echevarria, G., Sterckeman, T., Deng, T., Tang, Y., & Morel, J.-L. (2015). Weathering and vegetation controls on nickel isotope fractionation in surface ultramafic environments (Albania). *Earth Planet. Sci. Lett*., **423**, 24–35. https://doi.org/10.1016/j.epsl.2015.04.018

Fitton J. G. (1987) The Cameroon line, West Africa: a comparison between oceanic and continental alkaline volcanism. In *Alkaline Igneous Rocks, Geological Society Special Publications No. 30* pp. 273–291.

Fitton J. G. (2007) The OIB Paradox. In *Plates, Plumes, and Planetary Processes, Geological Society of America Special Paper 430* pp. 387–412.

Gale A., Dalton C. A., Langmuir C. H., Su Y. and Schilling J.-G. (2013) The mean composition of ocean ridge basalts. *Geochemistry, Geophys. Geosystems* **14**, 489–518.

Gall, L., Williams, H. M., Siebert, C., Halliday, A. N., Herrington, R. J., & Hein, J. R. (2013). Nickel isotopic compositions of ferromanganese crusts and the constancy of deep ocean inputs and continental weathering effects over the Cenozoic. *Earth Planet. Sci. Lett*., **375**, 148–155. https://doi.org/10.1016/j.epsl.2013.05.019

Gall, Louise, Williams, H. M., Halliday, A. N., & Kerr, A. C. (2017). Nickel isotopic composition of the mantle. *Geochim. Cosmochim. Acta*, 199, 196–209. https://doi.org/10.1016/j.gca.2016.11.016

Godard M., Awaji S., Hansen H., Hellebrand E., Brunelli D., Johnson K., Yamasaki T., Maeda J., Abratis M., Christie D., Kato Y., Mariet C. and Rosner M. (2009) Geochemistry of a long in-situ section of intrusive slow-spread oceanic lithosphere: Results from IODP Site U1309 (Atlantis Massif, 30°N Mid-Atlantic-Ridge). *Earth Planet. Sci. Lett*. **279**, 110–122.

Gueguen, B., & Rouxel, O. (2021). The Nickel isotope composition of the authigenic sink and the diagenetic flux in modern oceans. *Chem. Geol*, **563**, 120050. https://doi.org/10.1016/j.chemgeo.2020.120050

Gueguen, B., Rouxel, O., Ponzevera, E., Bekker, A., & Fouquet, Y. (2013). Nickel isotope variations in terrestrial silicate rocks and geological reference materials measured by MC-ICP-MS. *Geostand. Geoanalytical Res,* **37**(3), 297–317. https://doi.org/10.1111/j.1751-908X.2013.00209.x

Gueguen, B., Rouxel, O., Rouget, M. L., Bollinger, C., Ponzevera, E., Germain, Y., & Fouquet, Y. (2016). Comparative geochemistry of four ferromanganese crusts from the Pacific Ocean and significance for the use of Ni isotopes as paleoceanographic tracers. *Geochim. Cosmochim. Acta*, **189**, 214–235. https://doi.org/10.1016/j.gca.2016.06.005

Halliday A. N., Davidson J. P., Holden P., DeWolf C., Lee D.-C. and Fitton J. G. (1990) Trace-element fractionation in plumes and the origin of HIMU mantle beneath the Cameroon line. *Nature* **346**, 818–822.

Halliday A. N., Davies G. R., Lee D.-C. C., Tommasini S., Paslick C. R., Fitton J. G. and James D. E. (1992) Lead isotope evidence for young trace element enrichment in the oceanic upper mantle. *Nature* **359**, 623–627.

Halliday A. N., Dickin A. P., Fallick A. E. and Fitton J. G. (1988) Mantle dynamics: A Nd, Sr, Pb and O isotopic study of the Cameroon line volcanic chain. *J. Petrol*. **29**, 181–211.

973 Halliday A. N., Lee D.-C., Tommasini S., Davies G. R., Paslick C. R., Fitton J. G., James D. E., Fitton J. G. and
974 Dodie J. E. (1995) Incompatible trace elements in OIB and MORB and source enrichment in the sub-
975 oceanic mantle. *Earth Planet. Sci. Lett*. **133**, 379–395.

976 Hardarson B. S. and Fitton J. G. (1997) Mechanisms of crustal accretion in Iceland. *Geology* **25**, 1043–1046.

977 Harpp K. S. and White W. M. (2001) Tracing a mantle plume: Isotopic and trace element variations of
978 Galápagos seamounts. *Geochem Geophys Geosy* **2**(6), 1525-2027

979 Harvey J., Yoshikawa M., Hammond S. J. and Burton K. W. (2012) Deciphering the trace element
980 characteristics in Kilbourne Hole peridotite xenoliths: Melt-rock interaction and metasomatism
981 beneath the Rio Grande Rift, SW USA. *J. Petrol*. **53**, 1709–1742.

982 Hofmann, A., Bekker, A., Dirks, P., Gueguen, B., Rumble, D., & Rouxel, O. J. (2014). Comparing
983 orthomagmatic and hydrothermal mineralization models for komatiite-hosted nickel deposits in
984 Zimbabwe using multiple-sulfur, iron, and nickel isotope data. *Miner. Depos*, **49**(1), 75–100.
985 https://doi.org/10.1007/s00126-013-0476-1

986 Kempton P. D., Fitton J. G., Saunders A. D., Nowell G. M., Taylor R. N., Hardarson B. S. and Pearson G.
987 (2000) The Iceland plume in space and time: a Sr-Nd-Pb-Hf study of the North Atlantic rifted margin.
988 *Earth Planet. Sci. Lett.* **177**, 255–271.

989 Klaver, M., Ionov, D. A., Takazawa, E., & Elliott, T. (2020). The non-chondritic Ni isotope composition of
990 Earth's mantle. *Geochim. Cosmochim. Acta*, **268**, 405–421.
991 https://doi.org/10.1016/j.gca.2019.10.017

992 Lee, D.-C. (1994). A Chemical, Isotopic, and Geochronological Study of the Cameroon Line, West Africa.
993 University of Michigan.

994 Li, M., Grasby, S. E., Wang, S. J., Zhang, X., Wasylenki, L. E., Xu, Y., Sun, M., Beauchamp, B., Hu, D., & Shen,
995 Y. (2021). Nickel isotopes link Siberian Traps aerosol particles to the end-Permian mass extinction.
996 *Nat. Commun.,* **12**(1), 1–7. https://doi.org/10.1038/s41467-021-22066-7

997 Liang, Y.-H., Halliday, A. N., Siebert, C., Fitton, J. G., Burton, K. W., Wang, K.-L., & Harvey, J. (2017).
998 Molybdenum isotope fractionation in the mantle. *Geochim. Cosmochim. Acta*, **199**, 91–111.
999 https://doi.org/10.1016/j.gca.2016.11.023

1000 Muramatsu Y. (1983) Geochemical investigations from the Kimberley area, of kimberlites South Africa.
1001 *Geochem. J*. **17**, 71.

1002 Niu Y. and Batiza R. (1997) Trace element evidence from seamounts for recycled oceanic crust in the
1003 Eastern Pacific mantle. *Earth Planet. Sci. Lett*. **148**, 471–483. Available at:
1004 https://www.sciencedirect.com/science/article/pii/S0012821X97000484.

1005 Pašava, J., Chrastný, V., Loukola-Ruskeeniemi, K., & Šebek, O. (2019). Nickel isotopic variation in black
1006 shales from Bohemia, China, Canada, and Finland: a reconnaissance study. *Miner. Depos*, **54**(5), 719–
1007 742. https://doi.org/10.1007/s00126-018-0839-8

1008 Paslick C. R., Halliday A. N., James D. and Dawson J. B. (1995) Enrichment of the continental lithosphere by
1009 OIB melts: Isotopic evidence from the volcanic province of northern Tanzania. *Earth Planet. Sci. Lett.*
1010 **130**, 109–126.

1011 Porter, S. J., Selby, D., & Cameron, V. (2014). Characterising the nickel isotopic composition of organic-rich
1012 marine sediments. *Chem. Geol*, **387**, 12–21. https://doi.org/10.1016/j.chemgeo.2014.07.017

1013 Ratié, G., Jouvin, D., Garnier, J., Rouxel, O., Miska, S., Guimarães, E., Cruz Vieira, L., Sivry, Y., Zelano, I.,
1014 Montarges-Pelletier, E., Thil, F., & Quantin, C. (2015). Nickel isotope fractionation during tropical
1015 weathering of ultramafic rocks. *Chem. Geol*, **402**, 68–76.
1016 https://doi.org/10.1016/j.chemgeo.2015.02.039

1017 Ratié, G., Quantin, C., Jouvin, D., Calmels, D., Ettler, V., Sivry, Y., Vieira, L. C., Ponzevera, E., & Garnier, J.
1018 (2016). Nickel isotope fractionation during laterite Ni ore smelting and refining: Implications for
1019 tracing the sources of Ni in smelter-affected soils. *Appl. Geochemistry,* **64**, 136–145.
1020 https://doi.org/10.1016/j.apgeochem.2015.09.005

1021 Ratié, G., Quantin, C., Maia De Freitas, A., Echevarria, G., Ponzevera, E., & Garnier, J. (2019). The behavior
1022 of nickel isotopes at the biogeochemical interface between ultramafic soils and Ni accumulator
1023 species. *J. Geochemical Explor*, **196**, 182–191. https://doi.org/10.1016/J.GEXPLO.2018.10.008

1024 Revels, B. N., Rickli, J., Moura, C. A. V., & Vance, D. (2021). Nickel and its isotopes in the Amazon Basin: The
1025 impact of the weathering regime and delivery to the oceans. *Geochim. Cosmochim. Acta*, **293**, 344–
1026 364. https://doi.org/10.1016/j.gca.2020.11.005

1027 Ridley W. I. and Dawson J. B. (1975) Lithophile trace element data bearing on the origin of peridotite
1028 xenoliths, ankaramite and carbonatite from Lashaine volcano, N. Tanzania. *Phys. Chem. Earth* **9**, 559–
1029 569.

1030 Le Roex A. P., Bell D. R. and Davis P. (2003) Petrogenesis of group I Kimberlites from Kimberley, South
1031 Africa: Evidence from bulk-rock geochemistry. *J. Petrol*. **44**, 2261–2286.

1032 Saunders, N. J., Barling, J., Harvey, J., & Halliday, A. N. (2020). Heterogeneous nickel isotopic compositions
1033 in the terrestrial mantle – Part 1: Ultramafic lithologies. *Geochim. Cosmochim. Acta*, **285**, 129–149.
1034 https://doi.org/10.1016/j.gca.2020.06.029

1035 Spivak-Birndorf, L. J., Wang, S.-J., Bish, D. L., & Wasylenki, L. E. (2018). Nickel isotope fractionation during
1036 continental weathering. *Chem. Geol*, **476**, 316–326.
1037 https://doi.org/10.1016/J.CHEMGEO.2017.11.028

1038 Takano, S., Tanimizu, M., Hirata, T., Shin, K. C., Fukami, Y., Suzuki, K., & Sohrin, Y. (2017). A simple and rapid
1039 method for isotopic analysis of nickel, copper, and zinc in seawater using chelating extraction and
1040 anion exchange. *Anal. Chim. Acta*, **967**, 1–11. https://doi.org/10.1016/j.aca.2017.03.010

1041 Vance, D., Little, S. H., Archer, C., Cameron, V., Andersen, M. B., Rijkenberg, M. J. A., & Lyons, T. W. (2016).
1042 The oceanic budgets of nickel and zinc isotopes: the importance of sulfidic environments as
1043 illustrated by the Black Sea. *Philos. Trans. - R. Soc. London*, 374.
1044 https://doi.org/http://dx.doi.org/10.1098/rsta.2015.0294

1045 Wang, R.-M., Archer, C., Bowie, A. R., & Vance, D. (2019). Zinc and nickel isotopes in seawater from the
1046 Indian Sector of the Southern Ocean: The impact of natural iron fertilization versus Southern Ocean
1047 hydrography and biogeochemistry. *Chem. Geol*., **511**, 452–464.
1048 https://doi.org/10.1016/J.CHEMGEO.2018.09.010

1049 Wang, S.-J., Rudnick, R. L., Gaschnig, R. M., Wang, H., & Wasylenki, L. E. (2019). Methanogenesis sustained
1050 by sulfide weathering during the Great Oxidation Event. *Nat. Geosci*, 12(4), 296–300.
1051 https://doi.org/10.1038/s41561-019-0320-z

1052 Wang, S. J., Wang, W., Zhu, J. M., Wu, Z., Liu, J., Han, G., Teng, F. Z., Huang, S., Wu, H., Wang, Y., Wu, G., &
1053 Li, W. (2021). Nickel isotopic evidence for late-stage accretion of Mercury-like differentiated
1054 planetary embryos. *Nat. Commun*., **12**(1), 1–7. https://doi.org/10.1038/s41467-020-20525-1

1055 Workman R. K. and Hart S. R. (2005) Major and trace element composition of the depleted MORB mantle
1056 (DMM). *Earth Planet. Sci. Lett*. **231**, 53–72. Available at:
1057 https://www.sciencedirect.com/science/article/pii/S0012821X04007101.

1058 Xu Y. (2002) Evidence for crustal components in the mantle and constraints on crustal recycling
1059 mechanisms: Pyroxenite xenoliths from Hannuoba, North China. *Chem. Geol*. **182**, 301–322.

1060 Yi W., Halliday A. N., Alt J. C., Lee D.-C., Rehkamper M., Garcia M. O., Langmuir C. H. and Su Y. (2000)
1061 Cadmium, indium, tin, tellurium, and sulfur in oceanic basalts: Implications for chalcophile element
1062 fractionation in the Earth. *J. Geophys. Res*. **105**, 18927–18949.

1063 Yi W., Halliday A. N., Lee D.-C. and Christensen J. N. (1995) Indium and tin in basalts, sulfides, and the
1064 mantle. *Geochim. Cosmochim. Acta* **59**, 5081–5090.

1065